

Magnetic field configurations of a magnetar throughout its interior and exterior – core, crust and magnetosphere

Kotaro Fujisawa¹ * † & Shota Kisaka² ‡

¹*Advanced Research Institute for Science and Engineering, Waseda University, 3-4-1 Okubo, Shinjuku-ku, Tokyo 169-8555, Japan*

²*Institute of Particle and Nuclear Studies, KEK, 1-1 Oho, Tsukuba 305-0801, Japan*

Accepted 2014 September 10. Received 2014 August 25; in original form 2013 November 30

ABSTRACT

We obtained the magnetic field configurations, including both poloidal and toroidal components, throughout the interior and exterior of magnetars using a realistic equation of state. We divided the magnetized star into the hydromagnetic equilibrium core, Hall equilibrium crust and twisted force-free magnetosphere. We systematically and simultaneously calculated these regions under various boundary conditions using the Green function relaxation method, and noted the following interesting characteristics of these numerical results. First, the strength and structure of core magnetic fields affect the crustal magnetic fields. Second, the current sheet on the core-crust interface affects both internal and external magnetic field configurations. Third, the twisted magnetosphere makes a cross-point of magnetic field lines, such as X-point geometry, in the magnetosphere. The X-point geometry appears and disappears according to the strength of the twisted field in the magnetosphere or the core-crust boundary conditions. Our results mean that both Hall magnetohydrodynamics secular evolution and magnetospheric dynamical evolution are deeply affected by conditions of another region and the core-crust stress of magnetars.

Key words: stars: magnetic field; – stars: neutron; – stars: magnetars

1 INTRODUCTION

Neutron stars have the strongest magnetic fields among the stars in the universe. In particular, Anomalous X-ray Pulsars (AXPs) and Soft Gamma-ray Repeaters (SGRs) are considered to be magnetars, a special class of magnetized neutron stars. Magnetars have very strong dipole magnetic fields whose typical values reach approximately 10^{15} G at their surfaces. They display stationary intense emissions and dynamical flares releasing magnetic energy (Thompson & Duncan 1995). Such magnetic activities are also considered to be their heating source (Pons et al. 2007). The magnetic field configurations are important for such astrophysical events because the decay of magnetic energy deeply depends on their structure. Especially in relation to flares, both exterior and interior magnetic field structures are considered to be essential by many studies (e.g. Thompson & Duncan 2001; Thompson et al. 2002; Beloborodov & Thompson 2007; Masada et al. 2010). Recent studies have performed numerical simulations of crustal Hall magnetohydrodynamics (MHD) secular evolutions (Perna & Pons 2011) and strongly twisted force-free magnetospheric dynamical

evolutions (Parfrey et al. 2013) to understand the flares. However, since the magnetic field structures of the core-crust (interior) and magnetosphere (exterior) should be coupled, we must consider them simultaneously. As a first step, in this paper we will systematically and simultaneously calculate the equilibrium magnetic field structure of magnetars throughout their interior and exterior.

The Hall drift within the crust is considered to be vital for the internal field structure of magnetars. The Hall drift itself does not dissipate the magnetic fields, but produces higher order components of the magnetic field during the Hall cascade process. Such higher order components of the magnetic field promote Ohmic dissipation more efficiently (Jones 1988; Goldreich & Reisenegger 1992; Naito & Kojima 1994; Urpin & Shalybkov 1995; Shalybkov & Urpin 1997; Geppert & Rheinhardt 2002; Rheinhardt & Geppert 2002; Rheinhardt et al. 2004; Hollerbach & Rüdiger 2002; Hollerbach & Rüdiger 2004; Cumming et al. 2004; Reisenegger et al. 2007; Pons & Geppert 2007). The timescale of the Hall drift is determined by the strength of the magnetic fields within the crust. The Hall drift is characterized by the magnetic Reynolds number \mathcal{R}_m (Pons & Geppert

* E-mail: fujisawa@heap.phys.waseda.ac.jp

† Formerly at Department of Earth Science and Astronomy, Graduate School of Arts and Sciences, University of Tokyo, Komaba, Meguro-ku, Tokyo 153-8902, Japan

‡ Formerly at Institute for Cosmic Ray Research, University of Tokyo, 5-1-5 Kashiwa-no-ha, Kashiwa city, Chiba 277-8582, Japan

2007) as follows.:

$$\mathcal{R}_m \equiv \frac{t_{\text{Ohm}}}{t_{\text{Hall}}} = \frac{\sigma B}{ec n_e} \sim 10^3 \left(\frac{B}{10^{15} \text{G}} \right) \left(\frac{\sigma}{10^{25} \text{s}^{-1}} \right), \quad (1)$$

where t_{Ohm} and t_{Hall} are timescales of Hall drift and Ohmic dissipation, respectively. σ , c , n_e , and e are, respectively, the electrical conductivity of the crust, the speed of light, the electron number density, the charge of an electron. This value reaches approximately 1000 locally within the magnetar crust, because the crustal magnetic fields of the magnetar are sufficient large ($\geq 10^{15} \text{G}$). The Hall drift becomes very effective in the magnetar crust and its timescale is faster than or comparable to the lifetime of magnetars. Hall MHD numerical simulations have been performed (Kojima & Kisaka 2012; Viganò & Pons 2012; Viganò et al. 2012; Viganò et al. 2013; Gourgouliatos & Cumming 2014) and these works examined the Hall drift during the secular timescale.

As shown in recent works, the toroidal magnetic fields decrease rapidly during the Hall drift timescale because they are changed into higher order poloidal components by the Hall cascade, and Ohmic dissipation is promoted by the higher order components (Kojima & Kisaka 2012; Viganò et al. 2013; Gourgouliatos & Cumming 2014). According to these simulations, the Hall cascade becomes very effective when the initial energy of the toroidal magnetic field is much larger than that of the poloidal magnetic field. Therefore the energy ratio of the toroidal to the total magnetic field is a key factor in the secular evolution of the magnetic fields of magnetars. To investigate the magnetic field configurations of magnetars in equilibrium, we should include the Hall drift. One approach is the Hall equilibrium study.

Gourgouliatos et al. (2013) calculated Hall equilibria with both poloidal and toroidal magnetic fields by solving the Grad-Shafranov equation. They considered crustal magnetic fields in a Hall equilibrium and assumed a vacuum exterior. As Gourgouliatos et al. (2013) pointed out, the Hall equilibrium state is similar to the MHD equilibrium state which has been studied for sixty years since Chandrasekhar and his colleagues pioneering works (Chandrasekhar & Fermi 1953; Ferraro 1954; Chandrasekhar 1956; Chandrasekhar & Prendergast 1956; Prendergast 1956; Woltjer 1959a; Woltjer 1959b; Wentzel 1961; Ostriker & Hartwick 1968; Mikitinac 1973; Mikitinac 1975; Bocquet et al. 1995; Konno et al. 1999; Ioka & Sasaki 2004; Kiuchi & Yoshida 2008; Kiuchi & Kotake 2008; Haskell et al. 2008; Lander & Jones 2009; Ciolfi et al. 2009; Ciolfi et al. 2010; Duez & Mathis 2010; Fujisawa et al. 2012; Fujisawa et al. 2013; Fujisawa & Eriguchi 2013; Ciolfi & Rezzolla 2013). Both analytical and theoretical methods for the MHD equilibrium state were developed and investigated in these studies. Recently, some works considered more realistic and complex physical conditions in neutron star and magnetar interiors. Yoshida et al. (2012) considered stratification by chemical potentials in the neutron star interior and obtained stably stratified magnetized stars in general relativistic equilibrium. Lander et al. (2012) and Glampedakis et al. (2012) calculated magnetized neutron star equilibria with stratification and type II superconductivity in a Newtonian framework. Lander (2013) and Lander (2014) solved the superconducting flux tube tension and obtained magnetic field configurations of a neutron star with a superconducting core and a normal MHD crust by us-

ing a self-consistent field method. Glampedakis et al. (2014) have studied MHD magnetized star in equilibrium with twisted force-free magnetosphere by using a self-consistent field method. In their model, the interior field is in equilibrium with its magnetosphere. However, they did not employ a realistic equation of state (EOS) nor distinguish between its core and crust. Since the previous Hall MHD equilibrium (Gourgouliatos et al. 2013) study did not include a twisted magnetosphere, nobody has obtained magnetized equilibria throughout a core-crust-magnetosphere, which is essential for the progress of magnetar understanding.

In this paper, we extended the above works and systematically and simultaneously obtained the magnetic field structures across the core, crust, and magnetosphere for the first time. We used a realistic EOS to ensure that the core and crust are treated in an appropriate manner. We assumed crustal magnetic fields in the Hall equilibrium, because we considered a magnetar with a strong magnetic field where the Hall drift would be very effective within its crust. For simplicity, we assumed that the core is in MHD equilibrium. As described, the formulation of the Hall equilibrium state is very similar to the MHD equilibrium state (Gourgouliatos et al. 2013), but their physical meanings are different from each other. The MHD equilibrium state depends on mass density profiles because it describes the matter force balance. On the other hand, the Hall equilibrium state in the crust is determined by the electron number density distribution within the crust only and neglects the force balance of the crust. Therefore, the crust in this paper is elastic and stressed by Lorentz force of the crustal magnetic fields. In this paper, we assume that the magnetosphere is twisted and force-free. We adopted the equatorial shearing and ring models of Parfrey et al. (2013) as magnetospheric models. Since we are interested in the magnetosphere near the star, we neglected the rotation of the magnetosphere. In summary, we consider a MHD equilibrium core, Hall equilibrium crust and twisted force-free magnetosphere in this paper. This paper is organized as follows. In section 2, the basic equations and models are described. In section 3, we show the numerical results. We will provide discussion and our conclusion in section 4.

2 FORMULATION AND MODELS

2.1 Basic equations and integral forms

We consider the MHD equilibrium core, Hall equilibrium crust, and twisted force-free magnetosphere simultaneously in this paper. We use both spherical coordinates (r, θ, φ) and cylindrical coordinates (R, φ, z) . We assume that the system is stationary and axisymmetric. The magnetic fields are defined by two scalar potentials, Ψ and I , as

$$\mathbf{B} = \frac{1}{r \sin \theta} (\nabla \Psi \times \mathbf{e}_\varphi) + \frac{I}{r \sin \theta} \mathbf{e}_\varphi, \quad (2)$$

where Ψ is a poloidal magnetic flux function and I is a poloidal current density flux function. These magnetic fields components are related to the current density through the Maxwell Ampère equation as follows:

$$4\pi \frac{\mathbf{j}}{c} = \nabla \times \mathbf{B} = \frac{1}{r \sin \theta} (\nabla I \times \mathbf{e}_\varphi) - \frac{1}{r \sin \theta} \Delta^* \Psi \mathbf{e}_\varphi, \quad (3)$$

where Δ^* is the Grad-Shafranov operator below:

$$\Delta^* = \frac{\partial^2}{\partial r^2} + \frac{\sin \theta}{r^2} \frac{\partial}{\partial \theta} \left(\frac{1}{\sin \theta} \frac{\partial}{\partial \theta} \right). \quad (4)$$

To obtain the magnetized equilibria, we need to solve the following elliptic type equation:

$$\Delta^* \Psi = -4\pi r \sin \theta \frac{j_\varphi}{c}. \quad (5)$$

The right hand side of this equation contains the toroidal current density as a source term. This is derived from the matter equation in each region.

The Hall equilibrium state within the crust is described by the Hall equilibrium equation (Gourgouliatos et al. 2013 and App. A):

$$\nabla \times \left[\frac{c}{4\pi e n_e} \mathbf{B} \times (\nabla \times \mathbf{B}) \right] = 0. \quad (6)$$

This equation results in the following functional form of toroidal current density:

$$4\pi \frac{j_\varphi}{c} = \frac{I(\Psi)I'(\Psi)}{r \sin \theta} + 4\pi n_e r \sin \theta S(\Psi), \quad (7)$$

where $I(\Psi)$ and $S(\Psi)$ are arbitrary functions of Ψ , and $I' = \frac{dI}{d\Psi}$. The crustal toroidal current density is described by this equation.

As Gourgouliatos et al. (2013) pointed out, the toroidal current density in the Hall equilibrium system is similar to that of a barotropic MHD equilibrium system. The stationary MHD Euler equation without rotation and meridional flow is described as

$$\frac{1}{\rho} \nabla p = -\nabla \phi_g + \frac{1}{\rho} \left(\frac{\mathbf{j}}{c} \times \mathbf{B} \right), \quad (8)$$

where ρ , p , and ϕ_g are the mass density, pressure and gravitational potential, respectively. From the integrability condition of the Euler equation, we can obtain the relation

$$4\pi \frac{j_\varphi}{c} = \frac{I(\Psi)I'(\Psi)}{r \sin \theta} + 4\pi \rho r \sin \theta F(\Psi), \quad (9)$$

where $F(\Psi)$ is an another arbitrary function of Ψ . This equation expresses the core toroidal current density.

The twisted magnetosphere without rotation satisfies the force-free condition as

$$\frac{\mathbf{j}}{c} \times \mathbf{B} = 0. \quad (10)$$

Using this condition, we derived the functional form of toroidal current density as follows:

$$4\pi \frac{j_\varphi}{c} = \frac{I(\Psi)I'(\Psi)}{r \sin \theta}. \quad (11)$$

The toroidal current density in the magnetosphere is only described by the arbitrary function $I(\Psi)$.

We can calculate the magnetized equilibria using these functional forms of j_φ throughout the star. In order to easily include the boundary conditions, we calculated the integrated form of Eq. (5) using the Green function (see App. B),

$$\frac{\Psi(\mathbf{r})}{r \sin \theta} \sin \varphi = \frac{1}{c} \int_V \frac{j_\varphi(\mathbf{r}')}{|\mathbf{r} - \mathbf{r}'|} \sin \varphi' dV' + h.t.s, \quad (12)$$

where $h.t.s$ denotes the homogeneous terms of the Laplacian as shown below:

$$h.t.s = \sum_{n=1}^{\infty} \left(a_n r^n P_n^1(\cos \theta) + b_n r^{-n-1} P_n^1(\cos \theta) \right) \sin \varphi, \quad (13)$$

where $P_n^1(\cos \theta)$ are associated Legendre functions. The coefficients a_n and b_n are determined by the boundary conditions of Ψ . These homogeneous terms come from current sheets on the boundaries (see Fujisawa & Eriguchi 2013 and App. D).

The physical dimension of $F(\Psi)$ is different from $S(\Psi)$ because the dimensions of ρ and n_e differ (Gourgouliatos et al. 2013). Therefore, the functional form of $F(\Psi)$ can differ from $S(\Psi)$. On the other hand, the physical dimension of $I(\Psi)$ in each region is the same because this conserved quantity is only obtained from the axisymmetry condition (see App. A). We used the same functional form of $I(\Psi)$ in the core and crust regions.

2.2 Models of the internal magnetic field

We produced four models of the internal magnetic field according to the core-crust toroidal current density and boundary conditions. We must fix the functional forms of $I(\Psi)$, $F(\Psi)$, and $S(\Psi)$, and the current sheet on the core-crust boundary in order to achieve these models. The magnetic field configuration of each model is displayed in Fig. 1. Each model is described as follows:

(i) Model I is a purely crustal open magnetic field in a Hall equilibrium. Both poloidal and toroidal magnetic fields satisfy the Hall equilibrium state. This model is equivalent to the configurations used by Gourgouliatos et al. (2013). This model requires the opposite current sheet on the core-crust boundary to prevent the poloidal magnetic fields from entering the core (see App. D). The inner boundary conditions in this case are $\Psi = 0$ and $I = 0$ on the core-crust interface.

(ii) Model II is a purely crustal current model. The poloidal magnetic fields can penetrate the core region, but in this model, the toroidal magnetic field is confined within the crust region. The current density only exists within the crust. This model does not have the opposite current sheet on the core-crust boundary. Therefore, the core magnetic field is the inner vacuum solution of the crustal current. The inner boundary conditions in this model are $\Psi \neq 0$ and $I = 0$ on the core-crust interface.

(iii) Model III is a core-crust current model. Both poloidal and toroidal magnetic fields can exist in the core and crust regions. In other words, both poloidal and toroidal current densities can exist in the core and crust regions. In this model, the toroidal current density in the core flows in the same direction as the crust current. The inner boundary conditions in this model are $\Psi \neq 0$ and $I \neq 0$ on the core-crust interface.

(iv) Model IV is a core-crust current model. The toroidal current density in the core flows in the opposite direction to the crustal current in this model. The core magnetic fields' energy in this model is much larger than the crustal magnetic fields' energy, because such oppositely flowing toroidal current density makes the core magnetic fields' energy much larger (Fujisawa & Eriguchi 2013). The inner boundary conditions in this model are $\Psi \neq 0$ and $I \neq 0$ on the core-crust interface.

We calculated analytical solutions of these models without toroidal magnetic fields (see App. D). Models III and IV can have arbitrary current sheets on the core-crust boundaries. Such current sheets cause the arbitrary magnetic pressure on the bottom of the

crust (Braithwaite & Spruit 2006). We only calculated dipole current sheets in these models, but are also able to calculate the arbitrary higher order current sheet (see details of the current sheet in Fujisawa & Eriguchi 2013). The explicit form of the dipole toroidal current sheet j_s is

$$j_s = j_0 \delta(r - r_{\text{in}}) \sin \theta, \quad (14)$$

where r_{in} denotes the radius of crust-core interface and j_0 is the strength of the current density. δ is Dirac's delta function. This current sheet makes dipole magnetic fields (see the analytical solutions in App. D). We calculated solutions of model IV with and without current sheets in order to examine the influence of the current sheet. We calculated solutions of model IV with both positive and negative current sheets. Therefore, a total of 6 solution types for the models of the internal magnetic field are calculated in Sec. 3.1.

In order to achieve the core-crust conditions described, we choose the simplest forms (Gourgouliatos et al. 2013)

$$S(\Psi) = S_0, \quad (15)$$

$$F(\Psi) = F_0. \quad (16)$$

Although we can also compute more complex functional forms (see Fujisawa et al. 2012; Ciolfi & Rezzolla 2013), we used the simplest functional forms. We are interested in magnetic field configurations throughout the star and the influence of the boundary conditions. These functional forms were used to examine them easily and clearly. In particular, the values of S_0 and F_0 satisfy the conditions of $S_0 F_0 > 0$ (model III) and $S_0 F_0 < 0$ (model IV) in actual numerical computations.

We also chose the functional form of I to satisfy the boundary conditions on the stellar surface and the core-crust surface. If we assume that the magnetosphere is not twisted ($B_\varphi = 0$, outside the star), the toroidal current density must vanish outside the star ($I = 0$). We need to choose a functional form, such as the following (Tomimura & Eriguchi 2005)

$$I(\Psi) = \begin{cases} I_0(\Psi - \Psi_{\text{ex,max}})^{k+1} & (\Psi > \Psi_{\text{ex,max}}) \\ 0 & (\Psi \leq \Psi_{\text{ex,max}}) \end{cases}, \quad (17)$$

where $\Psi_{\text{ex,max}}$ is the maximum value of Ψ in the stellar exterior. We fixed the parameter $k = 0.1$ in all of our numerical computations. This choice of the parameter is exactly the same as in Yoshida & Eriguchi (2006) (also Yoshida et al. 2006; Lander & Jones 2009; Ciolfi et al. 2009; Fujisawa et al. 2012). As many previous works found, the choice of $k = 0.1$ results in locally strong toroidal magnetic fields.

The functional form of Eq. (17) is available in models I, III, and IV. When we calculated model II, we set $\Psi_{\text{ex,max}}$ as the maximum value of $\Psi_{\text{ex,max}}$ and $\Psi_{\text{c,max}}$, where $\Psi_{\text{c,max}}$ is the maximum value of Ψ in the core. If we choose this functional form, the current density vanishes outside the star and there is no toroidal magnetic field. This functional form always satisfies the boundary condition $I = 0$ at the stellar surface.

2.3 Models of a twisted magnetosphere

We calculated two types of twisted force-free magnetospheres: the equatorial shearing model and the ring model (see Parfrey et al.

2013). To obtain the equatorial shearing model, we chose the following functional form:

$$I(\Psi) = \begin{cases} I_0(\Psi - \Psi_{t,\text{min}})^{k+1} & (\Psi > \Psi_{t,\text{min}}) \\ 0 & (\Psi \leq \Psi_{t,\text{min}}) \end{cases}. \quad (18)$$

For the ring shearing model, we chose the following functional form:

$$I(\Psi) = \begin{cases} I_0(\Psi - \Psi_{\text{ex,max}})^{k+1} & (\Psi > \Psi_{\text{ex,max}}) \\ 0 & (\Psi_{\text{ex,max}} \leq \Psi \leq \Psi_{\text{ex,max}}) \\ I_1\{(\epsilon\Psi_{\text{ex,max}} - \Psi)(\Psi - \Psi_{t,\text{min}})\}^{k_2} & (\Psi_{t,\text{min}} \leq \Psi \leq \epsilon\Psi_{\text{ex,max}}) \\ 0 & (\Psi < \Psi_{t,\text{min}}) \end{cases}, \quad (19)$$

Here, I_1 , ϵ and k_2 are the parameters of a twisted magnetosphere. $\Psi_{t,\text{min}}$ denotes the minimum value of Ψ within the twisted magnetosphere. We defined the value of the maximum radius of the twisted field as r_M . The twisted field in the magnetosphere cannot exist beyond r_M . The regions of the twisted magnetosphere are limited by the last closed magnetic field line inside the radius r_M using these functional forms. When the twisted field in the magnetosphere is the ring model, the twisted field can exist within the limited region between the field lines $\Psi = \Psi_{t,\text{max}}$ and $\Psi = \epsilon\Psi_{\text{ex,max}}$ (see Eq. 19). The value of ϵ is bounded by $0 < \epsilon < 1$. This parameter determines the width of the twisted field region. We fixed $k_2 = 1.0$ and $\epsilon = 0.5$ in the ring model. We examined $k_2 > 1.0$ models, but did not obtain toroidal magnetic field solutions as strong as for $k_2 = 1.0$. As a result, we found that $k_2 = 1.0$ results in locally strong twisted magnetic fields within the ring regions.

2.4 Equation of state and numerical setting

We introduce a realistic EOS of neutron stars and a numerical setting. Glampedakis et al. (2014) used an $N = 1$ polytrope as a simple example of a neutron stars' EOS. They were not able to distinguish between the core and crust regions due to the simple polytropic EOS. Note that the magnetic field configurations in the equilibrium state depend on the distributions of mass density in the core and the electron number density within the crust (Eqs. 7 and 9). Therefore, realistic values of the size and the composition of the crust are required to calculate the equilibrium state of the crust and the core. We employed SLy EOS (Douchin & Haensel 2001) for our EOS. Since SLy EOS describes both the crust and the liquid core, it is suitable for the magnetar interior. This EOS can describe $\sim 2M_\odot$ neutron stars (Antoniadis et al. 2013; Demorest et al. 2010).

We fixed the maximum density $\rho_{\text{max}} = 1.0 \times 10^{15} \text{g/cm}^3$ and obtained the distributions of the mass density and electron number density (Fig. 2) using SLy EOS. The obtained stellar radius is $r_s \sim 1.17 \times 10^6 \text{cm}$ and the mass is $\sim 1.42M_\odot$. The radius of the core-crust interface r_{in} is $r_{\text{in}}/r_s \sim 0.923$ in this model, such that the thickness of the crust is approximately $\sim 8\%$ of the stellar radius. The electron number density at the base of the crust is $n_e \sim 2.67 \times 10^{36} \text{cm}^{-3}$ in this model. We defined $n_c \equiv 2.67 \times 10^{36} \text{cm}^{-3}$ as the maximum electron number density in our formulation. Noted that we assume the star is spherical in this paper, because the deformation due to magnetic fields is small, even a magnetar (Haskell et al. 2008; Ciolfi & Rezzolla 2013). Therefore, we used this spherical magnetar model in our numerical computations.

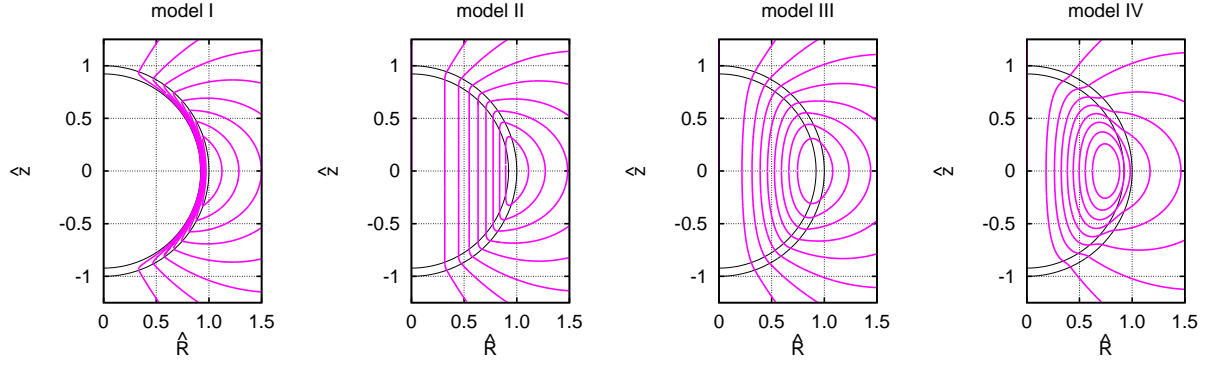


Figure 1. The contours of $\hat{\Psi}$ in each analytical model (see App. D). The inner curve is the core-crust boundary and the outer curve is the stellar surface. Model I: This model has purely crustal open magnetic fields. There is a negative current sheet on the core-crust boundary in order to exclude the core magnetic fields. Model II: This model has a purely crustal toroidal current. The core magnetic field is an inner vacuum solution of the crustal toroidal current. Model III: This model has both crustal and core toroidal currents. The configuration of the core magnetic field is different from Model II. Model IV: This model has opposite flowing toroidal current density. The core magnetic fields are stronger than crustal magnetic fields. The \hat{z} and \hat{R} denote dimensionless forms of z and R . We will define the dimensionless forms in Sec. 2.4.

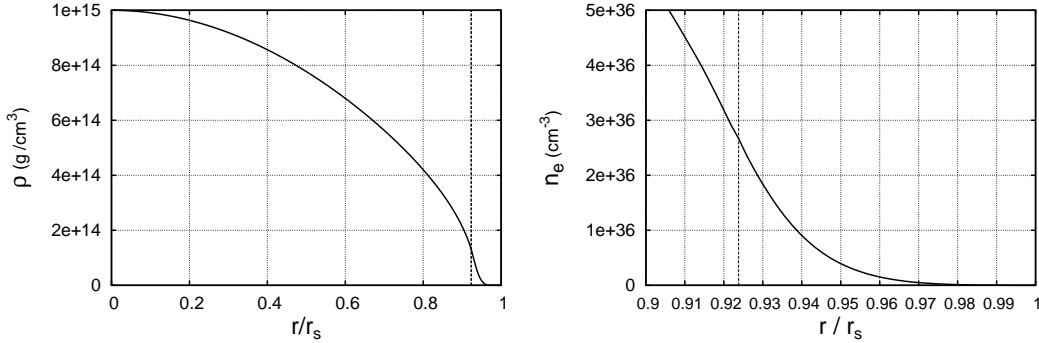


Figure 2. Mass density profile (left) and electron number density profile near the crust (right). The horizontal axis is normalized by the stellar radius r_s . Dashed lines correspond to the crust-core interface at $r_{\text{in}}/r_s \sim 0.923$.

To perform numerical computations properly, we introduced the following dimensionless physical quantities:

$$\hat{r} = \frac{r}{r_s}, \quad \hat{R} = \frac{R}{r_s}, \quad \hat{z} = \frac{z}{r_s}, \quad (20)$$

$$\hat{\rho} = \frac{\rho}{\rho_{\text{max}}}, \quad (21)$$

$$\hat{n}_e = \frac{n_e}{n_c}. \quad (22)$$

We need one more physical quantity in order to define dimensionless forms of other physical quantities. We chose S_{max} (the maximum value of S) as the physical quantity and defined the dimensionless \hat{S} as,

$$\hat{S} = \frac{S}{|S_{\text{max}}|}. \quad (23)$$

Using these four quantities, we can obtain the dimensionless magnetic energy:

$$\hat{E} = \frac{E}{r_s^5 n_c^2 S_{\text{max}}^2}. \quad (24)$$

We also show the forms of the other quantities in App. C. By using

these quantities, the functional forms of arbitrary functions also become dimensionless. Note that the value of \hat{S}_0 is 1 or -1 because of the functional form $S(\Psi) = S_0$ and the definition in Eq. (23).

In order to evaluate the energy ratio, we calculated the poloidal magnetic energy \hat{E}_p and the toroidal magnetic energy \hat{E}_t as

$$\hat{E}_p = \frac{1}{8\pi} \int (\hat{B}_r^2 + \hat{B}_\theta^2) d\hat{V}, \quad (25)$$

$$\hat{E}_t = \frac{1}{8\pi} \int \hat{B}_\varphi^2 d\hat{V}. \quad (26)$$

We defined the total magnetic energy $\hat{E} = \hat{E}_p + \hat{E}_t$. We also calculated the core magnetic energy (\hat{E}_{co}), the crust magnetic energy (\hat{E}_{cr}), and the stellar interior magnetic energy ($\hat{E}_{\text{st}} = \hat{E}_{\text{co}} + \hat{E}_{\text{cr}}$). Our numerical domain is defined as $0 \leq \theta \leq \pi$ in the angular direction with the stellar interior ($0 \leq \hat{r} \leq 1$) exterior magnetosphere ($1 \leq \hat{r} \leq 2$ for non-twisted magnetosphere models or $1 \leq \hat{r} \leq 16$ for twisted magnetosphere models) in the radial direction. We used a sufficient number of mesh points in this paper (see the analytical solutions in App. D and accuracy verification in App. E).

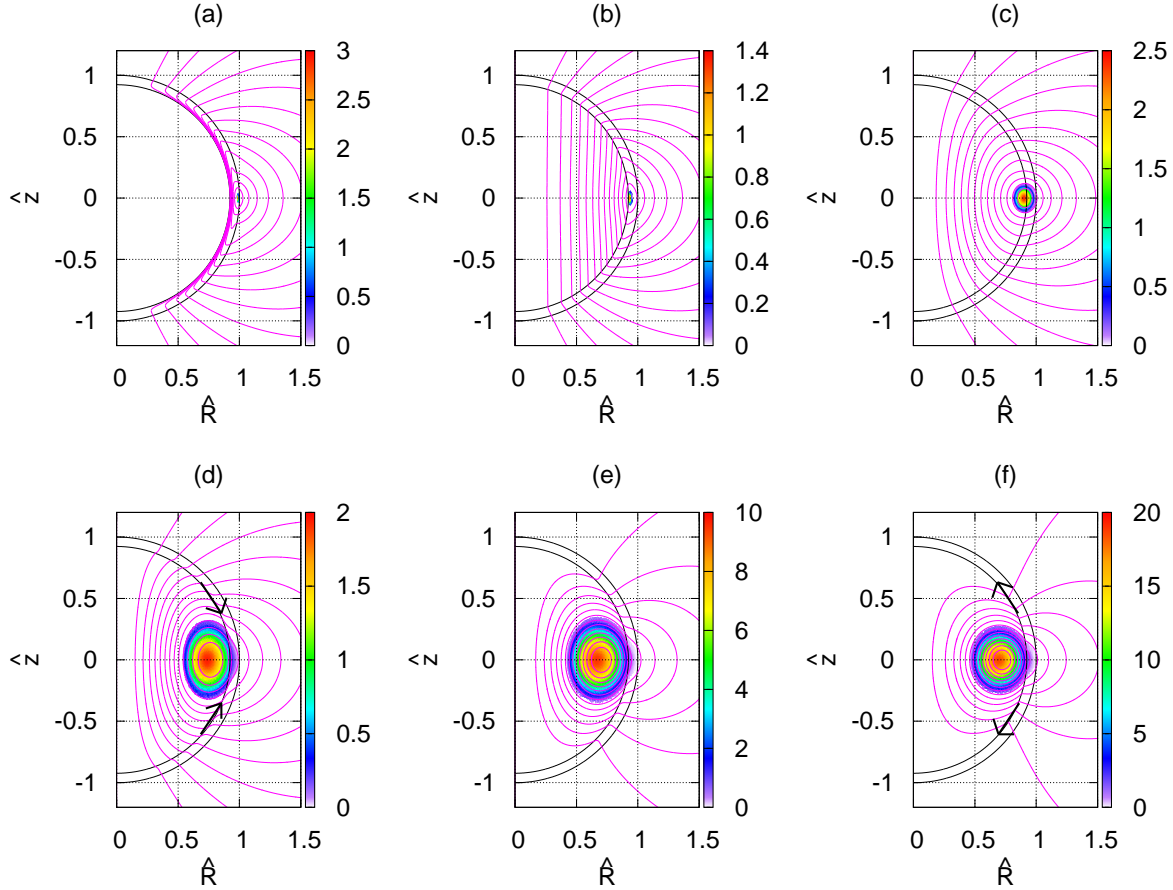


Figure 3. The contours of $\hat{\Psi}$ of each model (solid magenta lines). The black inner curve and the outer curve denote the core-crust boundary and the stellar surface, respectively. The colour maps denote the magnitude of the toroidal magnetic field \hat{B}_φ normalized by the strength of the dipole component at the north pole (\hat{B}_d). The arrows denote the directions of magnetic stress due to the current sheet.

	\hat{I}_0	\hat{S}_0	\hat{F}_0	model	E_{cr_t}/E_{cr}	E_{co_t}/E_{co}	E_{cr}/E	E_{co}/E	\hat{E}	\hat{B}_d	\hat{j}_0
(a)	800	1	0	I	1.23E-4	0.0	0.98	0.00	5.99E-5	3.55E-3	-
(b)	250	1	0	II	1.40E-2	0.0	0.08	0.67	3.27E-3	1.06E-1	-
(c)	30	1	1	III	1.14E-1	2.41E-2	0.07	0.74	3.27E-1	8.75E-1	0.0
(d)	10	-1	0.1	IV	4.09E-3	6.11E-2	0.08	0.83	1.88E-3	4.71E-2	0.1
(e)	10	-1	0.1	IV	7.73E-3	2.68E-1	0.02	0.95	9.83E-3	4.75E-2	0.0
(f)	10	-1	0.1	IV	1.62E-2	3.37E-1	0.02	0.96	8.81E-1	3.01E-1	-1.0

Table 1. Parameters and numerical solutions of the models. \hat{j}_0 denotes the strength of the current sheet on the core-crust interface. \hat{B}_d is the dimensionless strength of the dipole magnetic field.

3 RESULTS

3.1 Core-crust solutions with a non-twisted magnetosphere

First, we will show the solutions with a non-twisted magnetosphere ($\hat{B}_\varphi = 0$, outside the star). Since the toroidal magnetic field energy ratio (within the crust, E_{cr_t}/E_{cr}) relates to the Hall drift activity within the crust (Kojima & Kisaka 2012; Viganò et al. 2013), it is of interest to characterize the magnetized equilibrium states. We will focus on the energy ratios E_{cr_t}/E_{cr} in this paper. We computed many equilibria, changing the value of \hat{I}_0 for the 6 solutions types mentioned in Sec. 2.2. Each model displayed here has the

largest value of the energy ratio, E_{cr_t}/E_{cr} , for the present functional forms. We labelled the 6 obtained solutions (a) – (f) as follows: solution (a) model I type, solution (b) model II type, solution (c) model III type, solution (d) model IV type with a positive current sheet, solution (e) model IV type, solution (f) model IV type with a negative current sheet. The numerical solutions are tabulated in Tab. 1. The configurations of the poloidal and the toroidal magnetic fields are displayed in Fig. 3. The magnitude of the toroidal magnetic fields in Fig. 3 is normalized by that of the magnetic dipole component of each solution at the stellar north pole. As seen in Tab. 1, the energy ratio of the core (E_{co}/E) increases

sequentially from solution (a) to solution (f). The value reaches $E_{co}/E \sim 0.96$ in solution (f), while $E_{co}/E \sim 0.67$ in solution (b). Since solutions (d) and (f) have current sheets on the core-crust boundary, the poloidal field lines bend at this boundary. The direction of the bending depends on the sign of the current sheet. The direction of the magnetic stress due to the current sheet is plotted in Fig. 3.

The energy ratio E_{cr_t}/E_{cr} for each of the models is smaller than 0.5, such that the energy of poloidal components is dominant. However, the energy ratio changes according to the models. As seen in Tab. 1 and Fig. 3, the region of the toroidal magnetic field of solution (a) is very small, as is the energy ratio ($E_{cr_t}/E_{cr} \sim 10^{-4}$). This value is much smaller than in the solution by Gourgouliatos et al. (2013) because the width of the crust derived from a realistic EOS is smaller (see Fig. 9 in their paper). The energy ratio E_{cr_t}/E_{cr} of solution (b) is larger than that of solution (a). The toroidal magnetic field region also becomes slightly larger. Since the poloidal magnetic field lines penetrate the core region in this model, the $\hat{\Psi} \geq \hat{\Psi}_{\max}$ region within the crust becomes large (compare the analytical profiles of model I with model II in Fig. D1).

Solution (c) is a model III type solution with core toroidal current density. The energy ratio of the core (E_{co}/E) of solution (c) is larger than that of solution (b). The energy ratio (E_{cr_t}/E_{cr}) of solution (c) reaches 0.11 and is larger than those of solutions (a) and (b). On the other hand, the core toroidal magnetic fields are almost zero in solution (c). This numerical result shows that the core magnetic field structure is important when considering E_{cr_t}/E_{cr} in Hall equilibrium within the crust.

Solutions (d), (e), and (f) are model IV type solutions. They have opposite toroidal currents because the value of $\hat{F}_0 \hat{S}_0$ is always negative. As seen in Tab. 1, such oppositely flowing crustal toroidal current increases the core energy ratios (E_{co}/E & E_{co_t}/E_{co}). These tendencies are consistent with the arguments by Fujisawa & Eriguchi (2013). The ratios E_{co}/E reach approximately 0.8 – 0.9. These values are the largest among our solutions. These solutions also sustain the large toroidal magnetic field energy in the core region. The energy ratios (E_{co_t}/E_{co}) are $\sim 0.2 - 0.3$. The size of the toroidal magnetic field region within the crust of model IV solutions is slightly larger than those of any other solutions. The boundary conditions of \hat{I} at the core-crust boundary are $\hat{I} \neq 0$ and the values of \hat{I} continue smoothly at the boundary. These numerical results indicate that the $\hat{I} \neq 0$ boundary conditions on the core-crust boundary broaden the size of the toroidal magnetic field regions within the crust of the Hall equilibrium.

Solutions (d) and (f) have positive and negative current sheets on the core-crust boundary, respectively. Although the physical meaning and origin of the current sheet are unclear and difficult to understand in terms of micro physics (Lander 2013, 2014), we can regard the current sheet under the magnetic fields as magnetic stress on the bottom of the crust (Braithwaite & Spruit 2006). In this interpretation, the sign of the current sheet indicates the direction of the stress. The positive and negative current sheets denote the magnetic stresses in the direction of the equator and poles, respectively (see arrows in Fig. 3). As seen in Tab. 1, a positive current sheet decreases the energy ratio E_{co}/E (see solutions c and d), while a

negative current sheet increases the ratio E_{co}/E (see solutions (e) and (f)). Moreover, solution (d) has a smaller value of E_{cr_t}/E_{co} than solution (e). Solution (f) also has larger values of E_{cr_t}/E and E_{co_t}/E than solution (e). Note that the maximum magnitude of the core toroidal magnetic fields in solution (f) reaches approximately 20 times the size of its dipole magnetic component at the north pole (Fig. 3). This means that the current sheet (magnetic stress) at the bottom of the crust can sustain the strong core toroidal magnetic fields (see also Sec. 6.4 in Fujisawa & Eriguchi 2013). These results show that the core-crust stress affects the energy ratios of both crustal and core toroidal magnetic fields.

The energy ratio E_{cr_t}/E is affected by the boundary conditions and the core magnetic field configurations. This means that the Hall MHD evolution is strongly affected by core magnetic field conditions as per the recent numerical simulation by Viganò et al. (2013). We will discuss the influence of the boundary condition on the Hall MHD evolution in Sec. 4.1.

3.2 Solutions with an equatorial shearing magnetosphere

We calculated solutions with equatorial shearing using the functional form $\hat{I}(\hat{\Psi})$ in Eq. (18). First, we will show six solutions by changing the value of \hat{I}_0 . We used two types of internal magnetic field models (I, IV). Solutions (m-a), (m-b) and (m-c) have model I internal fields and solutions (m-d), (m-e) and (m-f) have model IV internal fields. Solutions (m-d), (m-e) and (m-f) do not have current sheets on the core-crust boundaries. The numerical results are tabulated in Tab. 2 and are displayed in Figs. 4 and 5. Three contours of $\hat{\Psi}$ – (m-d), (m-e), and (m-f) – and magnetospheric toroidal current distributions are displayed in Fig. 4. The arrow in the bottom left panel in Fig. 4 denotes the size of \hat{r}_M . The profiles of $\hat{\Psi}$ and the ratio of B_t to B_p on the equatorial plane are also displayed in Fig. 5. The equatorial shearing becomes larger as the value of \hat{I}_0 increases because the value of \hat{I}_0 represents the twisted strength (toroidal component) of the magnetic fields.

As seen in Fig. 4, the configuration of the poloidal magnetic field in the magnetosphere changes as shearing (the value of \hat{I}_0) increased. The poloidal magnetic field lines near the equatorial plane are stretched outward by the equatorial shearing current (compare (m-d) with (m-e) in Fig. 4). Since the energy ratio of stellar magnetic energy to the total magnetic energy E_{st}/E decreases as the value of \hat{I}_0 increases from Tab. 2, the value $E - E_{st}$ increases. We can see an interesting magnetic field structure near $\hat{r} \sim 3.3$ in Fig. 5 (solution (m-f)). As seen in the left panel, $\hat{\Psi}$ of solutions (m-d) and (m-e) decrease monotonically outside the star ($\hat{r} \geq 1$), but solution (m-f) has a local minimum near $\hat{r} \sim 3.3$ where the \hat{r} derivative of $\hat{\Psi}$ becomes 0. Since the sign of $\partial\hat{\Psi}/\partial\hat{r}$ represents the direction of \hat{B}_θ , the direction of the poloidal magnetic fields reverses at this point. Thus, the poloidal magnetic field lines cross and an X-point geometry forms at the point. We see X-points as singularities in Fig. 5. As the value of \hat{I}_0 increases, the magnitude of the twist ($|B_t/B_p|$) also increases (from (m-d) to (m-f) in the panels). If the twist reaches a critical value, the poloidal magnetic fields vanish and an X-point geometry forms. The inner singular point represents X-point geometry and the outer one represents the centre of the magnetic loop (see also solution (m-f) in Fig. 4). We define \hat{r}_X as the distance from the centre to the inner singular point.

	\hat{r}_M	\hat{I}_0	\hat{S}_0	\hat{F}_0	model	E_{cr}/E	E_{co}/E	E_{st}/E	\hat{E}	\hat{B}_d	\hat{r}_x
(m-a)	8.0	0.1	1.0	0.0	I	0.98	0.0	0.98	5.89E-5	3.41E-3	-
(m-b)	8.0	1.5	1.0	0.0	I	0.98	0.0	0.98	5.93E-5	3.47E-3	-
(m-c)	8.0	2.0	1.0	0.0	I	0.98	0.0	0.98	5.94E-5	3.48E-3	3.16
(m-d)	8.0	0.1	-1.0	0.5	IV	0.03	0.89	0.92	2.17E-2	1.47E-1	-
(m-e)	8.0	1.1	-1.0	0.5	IV	0.03	0.86	0.89	2.58E-2	1.70E-1	-
(m-f)	8.0	1.2	-1.0	0.5	IV	0.03	0.85	0.88	2.65E-2	1.73E-1	3.29

Table 2. Parameters and solutions with equatorial shearing models. Model I magnetic fields (m-a, m-b, m-c) and model IV magnetic fields (m-d, m-e, m-f) are tabulated.

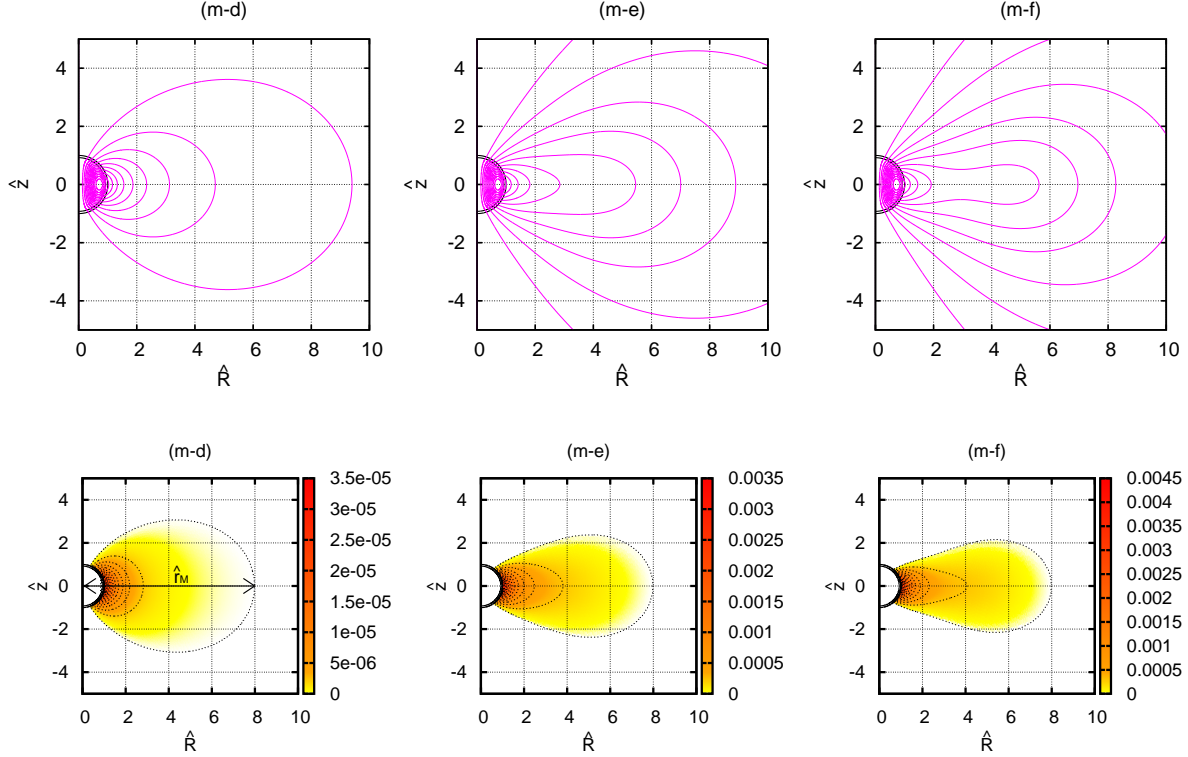


Figure 4. Top panels: The contours of $\hat{\Psi}$. Bottom panels: The colour maps and contours of \hat{j}_φ in a twisted magnetosphere. The inner circles in all panels denote core-crust interfaces and stellar surfaces. The X-point geometry appears at $\hat{r} \sim 3.29$ on the equatorial plane in solution (m-f) (top right panel). The arrow in the bottom left panel denotes the size of \hat{r}_M .

We can also find X-point geometry in solution (m-c). This X-point geometry of the poloidal magnetic field has not been seen in previous equilibrium studies (Glampedakis et al. 2014; Viganò et al. 2011) nor in the equilibrium models produced by a numerical simulation study (Parfrey et al. 2013). The X-point geometry would be unstable because it would cause magnetic reconnection as Parfrey et al. (2013) calculated. Our numerical result shows that the X-point geometry appears when the strength of the equatorial shearing (magnetospheric toroidal current density) exceeds a certain value.

Next, we calculated solutions with a current sheet on the core-crust interface and examined the influence of the current sheet on the X-point geometry. The X-point geometry is formed by the strong magnetospheric twisted field (magnetospheric toroidal current density) compared to the stellar magnetic fields (stellar toroidal

current density) (see the values E_{st}/E in Tab. 3). As we have seen, the large twisted field causes the X-point geometry as in solutions (m-c) and (m-f). On the other hand, the current sheet on the core-crust interface changes the stellar magnetic fields as shown in Sec. 3.1. Such current sheets can produce the X-point geometry. We calculated the solutions for both positive and negative current sheets and found that a positive current sheet tends to form an X-point geometry. We show three solutions – (s-a), (s-b), and (s-c) with model IV core magnetic fields. We calculated them using the same parameters, apart from the strength of the current sheet on the core-crust boundary \hat{j}_0 . The numerical results are tabulated in the upper column of Tab. 3 and are displayed in Fig. 6. Fig. 7 shows the ratio of B_t to B_p on the equatorial surface. The maximum value of $|B_t/B_p|$ for solution (s-b) is approximately 100. This value is much larger than that of solution (m-e) which has the same internal

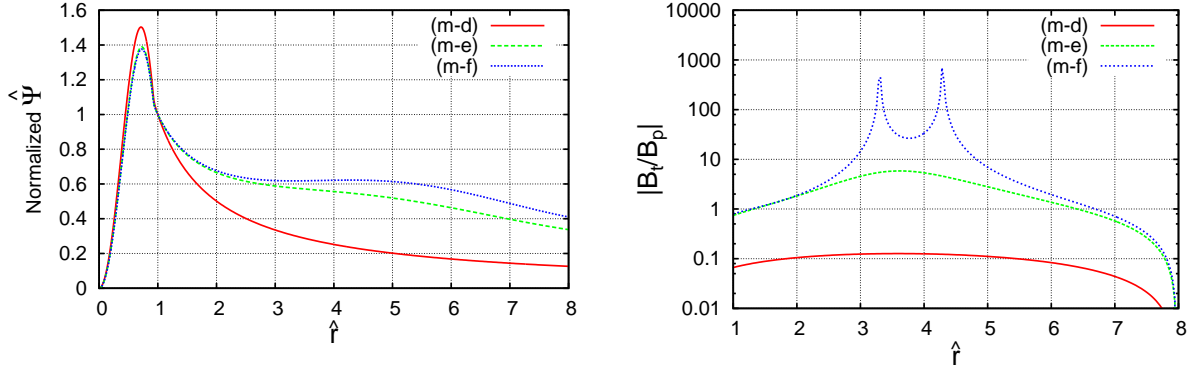


Figure 5. Left panel : The profiles of Ψ normalized by the surface value on the equatorial plane. Each line denotes solution (m-d) (solid line), solution (m-e) (dashed line), and solution (m-f) (dotted line). Solution (m-d) and solution (m-e) decrease monotonically in the magnetosphere ($\hat{r} > 1$), but solution (m-f) has a local maximum value at $\hat{r} \sim 3.29$. Right panel : The ratios of the toroidal component and the poloidal component $|B_t/B_p|$. These values represent the strength of the twist of the fields. Solution (m-f) has two singular points at $\hat{r} \sim 3.29$ and $\hat{r} \sim 4.2$. The first singular point comes from the X-point geometry and the second point comes from the magnetic neutral point (see Fig. 4)

	\hat{r}_M	\hat{I}_0	\hat{S}_0	\hat{F}_0	model	E_{cr_t}/E	E_{co_t}/E	E_{cr}/E	E_{co}/E	E_{st}/E	\hat{E}	\hat{B}_d	\hat{r}_X	\hat{j}_0
(s-a)	8.0	1.1	-1	0.5	IV	5.89E-2	2.50E-2	0.03	0.86	0.89	2.58E-2	1.70E-1	-	0.0
(s-b)	8.0	1.1	-1	0.5	IV	7.06E-2	1.56E-2	0.06	0.67	0.73	1.42E-1	6.15E-1	-	0.5
(s-c)	8.0	1.1	-1	0.5	IV	7.20E-2	1.36E-2	0.07	0.65	0.72	2.75E-1	8.82E-1	3.34	0.8
(e-a)	4.0	2.5	-1.0	0.5	IV	8.14E-2	3.50E-2	0.03	0.80	0.83	3.32E-2	2.10E-1	1.59	
(e-b)	8.0	1.2	-1.0	0.5	IV	6.08E-2	2.71E-2	0.03	0.85	0.88	2.65E-2	1.73E-1	3.29	
(e-c)	15.0	0.75	-1.0	0.5	IV	3.53E-2	1.53E-2	0.03	0.87	0.90	2.38E-2	1.56E-1	6.04	

Table 3. Parameters and solutions with a equatorial models. Solutions with current sheet – (s-a, s-b, s-c) – and without a current sheet changing the value of \hat{r}_M – (e-a), (e-b), (e-c) – are tabulated.

field model and no current sheet. From Fig. 5, the critical value of $|B_t/B_p|$ would be approximately 100.

As seen in Tab. 3, the positive current sheet decreases the stellar magnetic field energy ratio (see E_{st}/E). Thus, the value of $E - E_{st}$ is increased by the positive current sheet. As a result, an X-point geometry is formed within the twisted region in solutions (s-c) (see Fig. 7). The positive current sheet has magnetic pressure as solution (d) in Fig. 3. These numerical results imply that the core-crust boundary condition and the magnetic pressure can change the magnetospheric configurations and cause an X-point geometry within the twisted region. We discuss X-point geometry in Sec. 4.2.

Finally, we observed the internal magnetic field configurations changing the size of the twisted-magnetosphere (the value of \hat{r}_M). We calculated three solutions (e-a) ($\hat{r}_M = 4.0$), (e-b) ($\hat{r}_M = 8.0$), and (e-c) ($\hat{r}_M = 15.0$) with model IV internal magnetic fields. The numerical solutions are tabulated in the lower column of Tab. 3 and are displayed in Fig. 8. Figure 8 shows the contours of $\hat{\Psi}$ (poloidal magnetic field) and B_φ (colour map) normalized by the strength of the surface dipole field. As seen in Fig. 8, the size of the toroidal magnetic field region within the crust becomes much larger than those without a magnetosphere (compare with Fig. 3). As the size of the twisted field increases (sequentially from (e-a) to (e-c)), the size of the toroidal magnetic field region within the crust also increases. As seen in Tab. 3, however, the energy ra-

tios E_{cr_t}/E_{cr} and E_{co_t}/E_{co} decrease as \hat{r}_M increases. Since the boundary condition of \hat{I} on the stellar surface is $\hat{I} \neq 0$ in the region ($\hat{\Psi} > \hat{\Psi}_{t,max}$), the boundary condition $\hat{I} \neq 0$ significantly broadens the size of the toroidal magnetic field region within the crust.

All solutions (e-a), (e-b), and (e-c) have X-point geometries. The energy ratio E_{st}/E increases from 0.83 (e-a) to 0.90 (e-c) as the size of the twisted field region becomes large. In other words, the value of $E - E_{st}$ for solution (e-a) is larger than for solutions (e-b) and (e-c). This result implies that the star requires a stronger magnetospheric energy (twist) to make an X-point geometry near the stellar surface as in solution (e-a). We see this tendency in following subsection.

3.3 Solutions with a ring shearing magnetosphere

Finally, we calculated magnetized equilibria of model IV internal magnetic fields with a ring shearing magnetosphere (Parfrey et al. 2013). The numerical results are tabulated in Tab. 4 and are shown in Fig. 9. The twisted region is limited between the field lines $\hat{\Psi} = \hat{\Psi}_{t,max}$ and $\hat{\Psi} = \hat{e}\hat{\Psi}_{ex,max}$ (see Eq. 19). The toroidal current density of the ring model has both positive and negative values (see bottom panels in Fig. 9) in the magnetosphere. This distribution is similar to the solutions by Parfrey et al. (2013) (see figure 4 in their paper). The energy ratio E_{cr_t}/E_{cr} of solutions (r-b), (r-c),

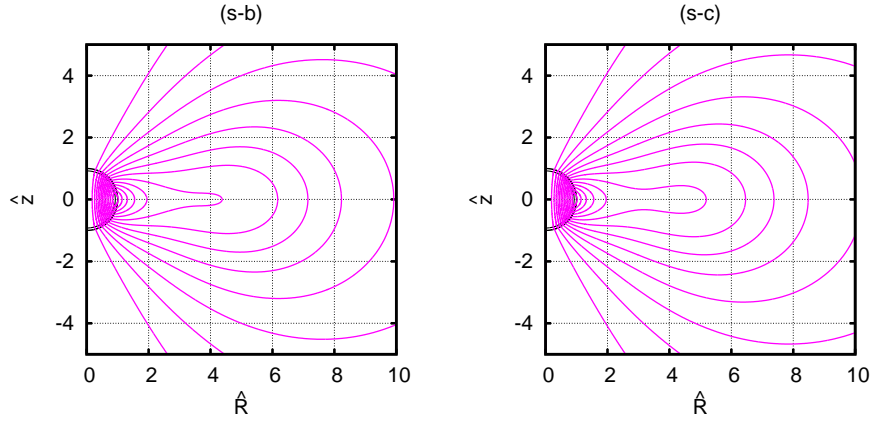


Figure 6. The contour of $\hat{\Psi}$. The inner circles in the top panels denote stellar surfaces. An X-point geometry appears at $\hat{r} \sim 3.34$ in solution (s-c).

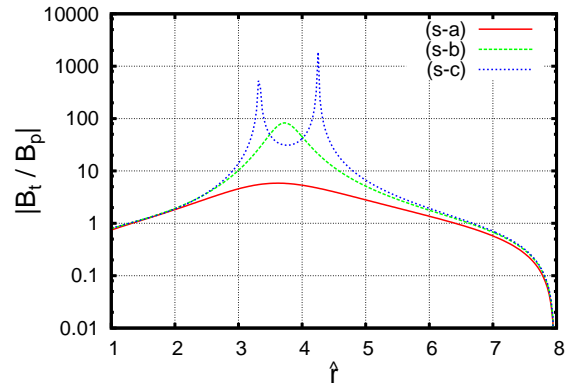


Figure 7. The ratios of the toroidal component to the poloidal component $|B_t/B_p|$. The figure shows solution (s-a) (solid line), solution (s-b) (dashed line), and solution (s-c) (dotted line).

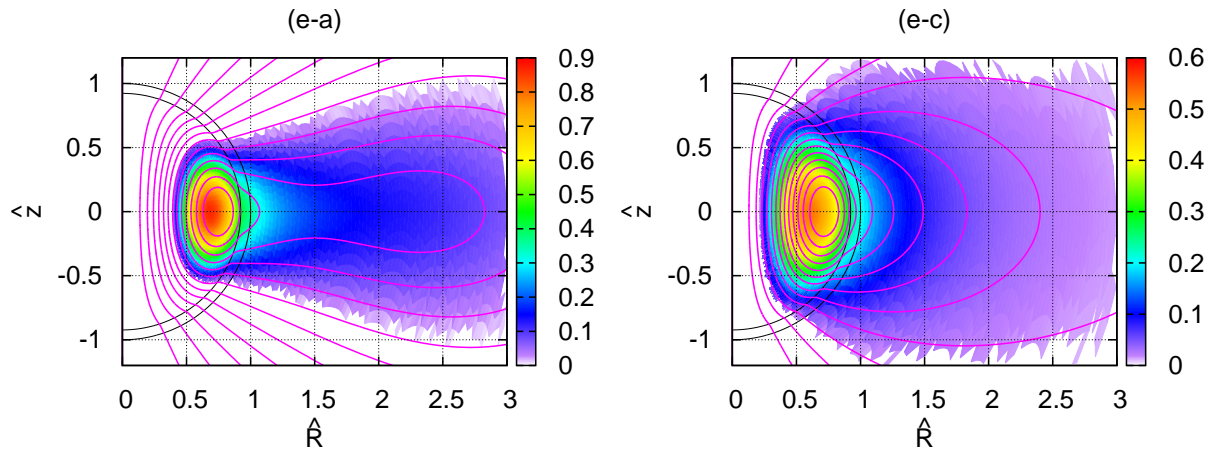


Figure 8. The counter of $\hat{\Psi}$ (solid line) and the distribution of B_φ (colour map) normalized by the magnetic dipole component strength at the north pole. The toroidal magnetic field region within the crust becomes larger as the size of the magnetosphere increases. Both solution (e-a) and solution (e-c) have X-point geometry fields near $\hat{r} \sim 1.59$ for solution (e-a) and $\hat{r} \sim 6.04$ for solution (e-c).

	\hat{r}_M	\hat{I}_0	\hat{I}_1	\hat{S}_0	\hat{F}_0	model	E_{ct_t}/E_{cr}	E_{co_t}/E_{co}	E_{cr}/E	E_{co}/E	E_{st}/E	\hat{E}	\hat{B}_d	\hat{r}_X
(r-a)	1.0	10	0.0	-1.0	0.1	IV	7.37E-3	2.68E-1	0.02	0.95	0.97	9.85E-3	4.75E-2	-
(r-b)	4.0	10	250	-1.0	0.1	IV	7.82E-3	2.68E-1	0.02	0.95	0.97	9.76E-3	4.74E-2	-
(r-c)	8.0	10	120	-1.0	0.1	IV	7.53E-3	2.68E-1	0.02	0.95	0.97	9.76E-3	4.74E-2	-
(r-d)	15.0	10	80.0	-1.0	0.1	IV	7.48E-3	2.68E-1	0.02	0.95	0.97	9.80E-3	4.74E-2	6.33

Table 4. Parameters and solutions of ring shearing models (r-a), (r-b), (r-c), and (r-d).

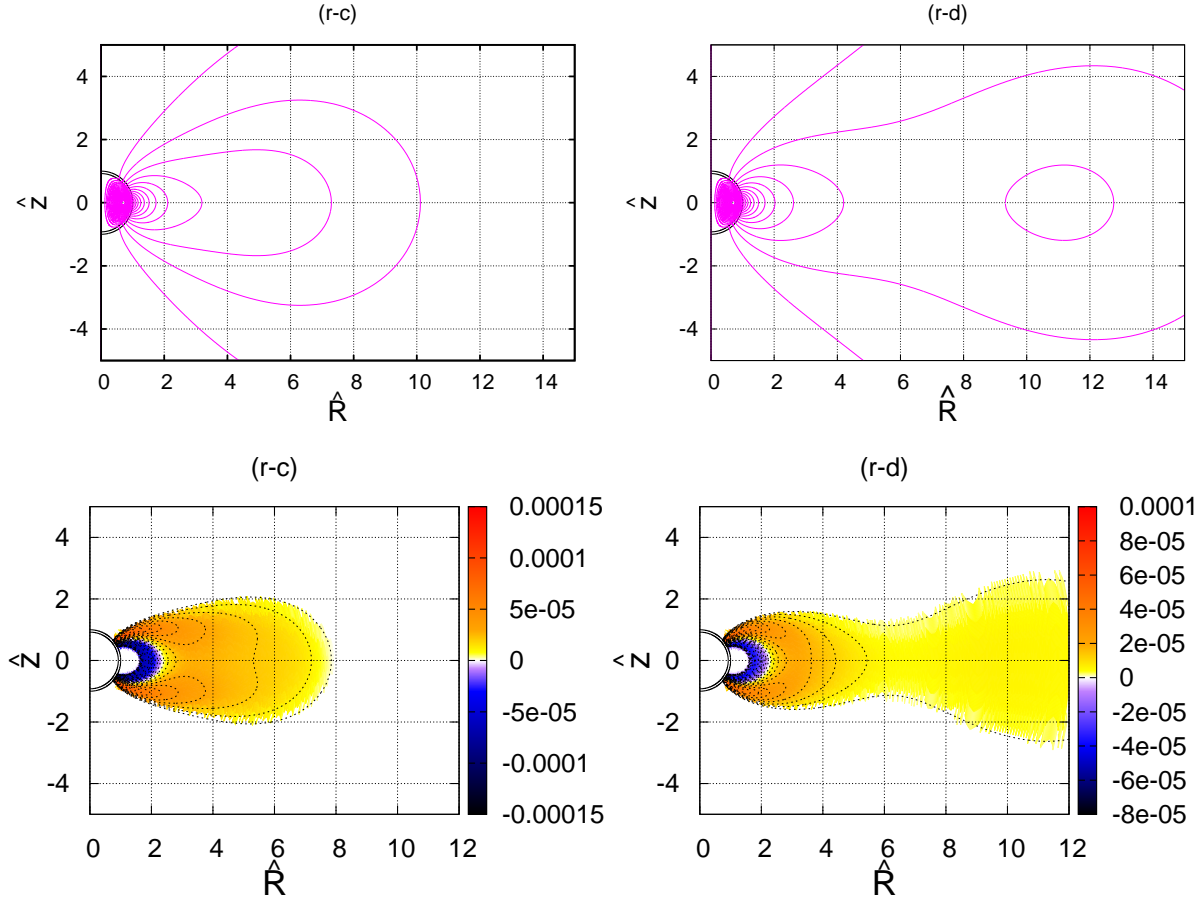


Figure 9. Top panels: The contour of $\hat{\Psi}$. Bottom panels: The colour maps and contours of \hat{j} in a twisted magnetosphere. The inner circles in all panels denote stellar surfaces. While an X-point geometry appears $\hat{r} \sim 6.33$ in solution (r-d) (right panels), solution (r-c) do not have X-point geometry (left panel). The ring shearing models have both positive and negative toroidal current density in the magnetosphere.

and (r-d) are almost the same as for solution (r-a). The magnetospheric toroidal current density near the star is much smaller than that of the equatorial model (see solution (e-c) in Fig. 8) because the magnetospheric toroidal current is limited within the narrow regions and takes both positive and negative values. The ring shearing magnetosphere in this paper does not significantly influence the internal magnetic field configurations.

We cannot obtain solutions with X-point geometry within $\hat{r}_M < 15$ in this paper because the magnetospheric toroidal current density within the ring shearing model is much smaller than in the equatorial shearing model. Solutions (r-b) and (r-c) do not have X-point geometries. A large size of the twisted region is required in order to form the X-point geometry. An X-point geometry ap-

pears only when the size of the twisted field region is sufficiently large such as in solution (r-d) ($\hat{r}_M = 15$) in our numerical results. These results show that an X-point geometry of the ring shearing model in this paper cannot appear near the stellar surface, unlike for the equatorial shearing models. The X-point geometry in the ring shearing model tends to appear in the outer region of the equatorial shearing X-point geometry. The minimum value of \hat{r}_X in the ring shearing model is larger than for the equatorial shearing model in these calculations. This result means that the minimum value of \hat{r}_X changes according to the shearing model and the size of the twisted field in the magnetosphere.

4 DISCUSSION AND CONCLUDING REMARKS

4.1 The influence of boundary conditions on the Hall MHD evolution

The boundary conditions of the crust play very important roles in the Hall MHD secular evolutions. Very recently, Viganò et al. (2013) performed Hall MHD simulations under three types of core magnetic fields models (see Fig.2 in Viganò et al. 2013). They showed that the evolutionary path is affected by the core magnetic field. We will now discuss the influence of the core magnetic fields on the crustal magnetic fields in Hall equilibrium using our equilibrium solutions.

We calculated 6 solutions and found that the Hall equilibrium state within the crust is significantly affected by the core-crust and the stellar surface-magnetosphere boundary conditions. As we have seen in Sec. 3.1, the presence of the core magnetic field changes the crustal magnetic field in the Hall equilibrium (solutions (c)). Moreover, the strong core toroidal magnetic field broadens the regions of the crustal toroidal magnetic field in the Hall equilibrium (solution (e)). The surface boundary condition also changes the crustal magnetic field configurations. Additionally, the twisted magnetosphere around the star increases the size of the crustal toroidal magnetic fields. These boundary condition affect the Hall cascade during the secular magnetic field evolution, because the dissipation timescale of the current sheet is larger than the Hall timescale (App. F).

The initial large toroidal magnetic fields strengthen the Hall drift activity (Kojima & Kisaka 2012; Gourgouliatos & Cumming 2014). If the crustal magnetic fields are large enough to drive the Hall cascade very effectively ($\geq 10^{15}$ G), the timescale of the Hall drift is much faster than the Ohmic timescale (see Eq. 1). In this case, the Hall drift would stop when the initial toroidal magnetic fields have been changed into poloidal components by the Hall cascade and have reached Hall equilibrium configurations. Therefore, the energy ratio E_{cr_t}/E_{cr} of the Hall equilibria would represent the efficiency of the Hall cascade if the magnetar has strong initial toroidal component magnetic fields at the beginning of the Hall MHD secular evolution.

The initial magnetic field configurations in the magnetar interior are still unclear, but they would have strong toroidal magnetic fields because of the rapid differential rotation (Duncan & Thompson 1992; Spruit 2009). The magnetar would be in a stable MHD equilibrium state because the Alfvén timescale ($= \sqrt{4\pi\rho}r_s/B \sim 0.1$ s for a typical magnetar with magnetic fields in the order of $B = 10^{15}$ G) is much faster than the dynamical and crust forming timescales. The MHD equilibria with strong toroidal magnetic fields would be dynamically stable because they satisfy Braithwaite’s stability criterion (Braithwaite 2009; Duez et al. 2010):

$$a \frac{E}{|W|} < \frac{E_p}{E} \leq 0.8, \quad (27)$$

where $E/|W|$ is the ratio of magnetic energy to gravitational energy. a is a certain dimensionless factor in the order of 10^3 for neutron stars. Since the value of $E/|W|$ is smaller than $\sim 10^{-5}$ for typical magnetars, the left-hand side of this inequality (Eq. 27) could be less than approximately 10^{-2} . Therefore, this criterion means the configurations are dynamically stable even if the toroidal

magnetic fields are much stronger than the poloidal magnetic fields. As a result, it is natural that the magnetar has strong initial toroidal magnetic fields in its interior.

Here, we assume that the magnetar has very large strong initial toroidal magnetic fields and that the toroidal magnetic fields are changed into poloidal components by the Hall cascade until the system reaches the Hall equilibrium state. This situation is different from initial models in Viganò et al. (2013) because except for A14T in their paper, their initial models do not have toroidal magnetic fields. If the value of E_{cr_t}/E_{cr} in the Hall equilibrium is very small ($\sim 0.1\%$), the Hall drift would be effective because almost of the initial toroidal components are changed into poloidal components by the Hall drift. On the other hand, if the value of E_{cr_t}/E_{cr} in Hall equilibrium is not small ($\sim 10\%$), the Hall drift would be less effective. Therefore, we can evaluate the efficiency of the Hall drift using the toroidal magnetic field energy ratio of each solutions.

The Hall drift of model I, such as in solution (a), would be very active because most toroidal magnetic field components would change to poloidal magnetic field components. This is consistent with the calculations by Kojima & Kisaka (2012) (see the left panel of Fig.5 in Kojima & Kisaka 2012). In contrast, the value of the energy ratio E_{cr_t}/E_{cr} of solution (c) is much larger than that of solution (a). These numerical results mean that the Hall cascade in such configurations would be more passive than the configuration in solution (a). Therefore, the presence of the core magnetic fields tends to weaken the Hall drift within the crust region.

The crustal magnetic field in the Hall equilibrium with a twisted-magnetosphere also has a very large toroidal magnetic field region. Since the size of the toroidal magnetic field region of the equatorial twisted model is much larger than that of the non-twisted model, the Hall cascade with a twisted magnetosphere would decrease. We see the same tendency in Sec. 2.1.2 of Pons & Geppert (2007). They calculated force-free boundary models and argued that the Hall drift within the crust is reduced by the twisted magnetosphere.

4.2 Magnetic X-point geometry and flare

We have calculated core-crust magnetic field configurations with a twisted force-free magnetosphere. We found interesting poloidal magnetic field configurations in the magnetosphere. When the magnetospheric toroidal current density is relatively large, a magnetic X-point geometry is formed in the equatorial plane of the magnetosphere. This X-point geometry is constituted by anti-parallel poloidal magnetic fields around the point. These anti-parallel magnetic fields would cause a magnetic reconnection and result in a giant flare of the magnetar (Masada et al. 2010; Parfrey et al. 2013). The distance of the X-point geometry changes as a result of the shearing models. The equatorial shearing model can cause an X-point geometry near the stellar surface and the minimum value of \hat{r}_X is ~ 1.59 as in solution (e-a) (Tab.1). In contrast, the ring shearing model cannot make an X-point geometry near the stellar surface and the minimum value of \hat{r}_X is ~ 6.33 in solution (r-d) (Tab. 3). The location of the magnetic reconnection in the magnetosphere would deeply depend on the magnetospheric models.

Next, we considered the physical process for an X-point ge-

ometry. We obtained an X-point geometry by changing three parameters. An X-point geometry appears by condition (1) increasing the value of toroidal magnetic fields (\hat{I}_0) (solutions (m-c) and (m-f)), condition (2) increasing the strength of the current sheet (\hat{j}_0) on the core-crust boundary (solution (s-c)), and condition (3) increasing the size of the twisted magnetosphere (\hat{r}_M) (the size of the surface toroidal magnetic field) (solution (r-d)).

Condition (1) is satisfied in the case where the magnetospheric toroidal current is accumulated by the fixed stellar current (Parfrey et al. 2013). Then, the value of \hat{I}_0 increases as the energy of the toroidal magnetic field in the magnetosphere increases. Condition (2) is satisfied in the case where the internal magnetic field configurations and elastic force balance in the crust are changed by dynamical events such as a glitch or elastic crust cracking. Since these events would change the core-crust boundary condition, the value of \hat{j}_0 varies in this case as we have changed the current sheet on the boundary. Condition (3) is satisfied in the case where the toroidal magnetic fields emerge from the crust. The size of the surface toroidal magnetic fields (twisted magnetosphere) is enlarged because we have changed the value of \hat{r}_M . The large crust cracking would result in the toroidal magnetic fields emerging. Such cracking releases stress on the crust and decreases the negative current sheet on the core-crust boundary. During this process, the internal magnetic field configurations would change from a configuration as per solution (f) to a configuration as per solution (d). The direction of the magnetic pressure also changes as seen in Fig. 3. The strength of the negative current sheet (\hat{j}_0) decreases and the strength of the positive current sheet increases during this process. Since the energy ratio E_{co_t}/E_{co} decreases from solutions (f) to (d), the core toroidal magnetic field would be ejected from the star (Thompson & Duncan 2001; Fujisawa & Eriguchi 2013). At the same time, the twist of the magnetosphere would increase as seen in Fig. 6, because the strength of the positive current sheet (\hat{j}_0) is increasing. It is probable that such toroidal magnetic energy injection would make giant magnetic loops (Gourgouliatos & Lynden-Bell 2008; Takahashi et al. 2009, 2011; Matsumoto et al. 2011). These dynamical events in the stellar interior and the changes of the toroidal magnetic field on the surface would result in a reconnection within the magnetosphere and a giant flare. Our numerical results would be a key to understanding the physical mechanisms of a magnetar's giant flare.

4.3 Concluding remarks

We systematically and simultaneously calculated magnetized equilibria throughout an MHD equilibrium core, Hall equilibrium crust, and twisted force-free magnetosphere with both poloidal and toroidal magnetic fields using the Green function method under various boundary conditions. We employed SLy EOS as a realistic equation of state in order to treat the core and crust consistently. We found that the magnetic field configuration in each region is deeply affected by the other.

We found that the Hall equilibrium state is significantly affected by both inner (core) and outer (twisted-magnetosphere) boundary conditions. The core magnetic field configurations influence the crustal toroidal magnetic field. The crustal magnetic fields, such as in the model with a purely crustal magnetic field

(solution (a)) have the smallest toroidal magnetic field energy ratio among all of our solutions. In contrast, the core magnetic fields of solutions such as solution (c) sustain the larger toroidal magnetic field energy ratio (E_{cr_t}/E_{cr}) within the crust in the Hall equilibrium. The twisted force-free magnetosphere also widens the size of the crustal toroidal magnetic field region. We can evaluate the efficiency of the Hall cascade using the toroidal magnetic field energy ratio E_{cr_t}/E_{cr} in the Hall equilibrium. The presence of the core magnetic fields would weaken the efficiency of the Hall cascade because the crustal toroidal magnetic field energy is not small when the crustal magnetic fields reach the Hall equilibrium. Since the twisted magnetosphere widens the size of the crustal toroidal magnetic field region, it also weakens the Hall cascade within the crust.

The magnetosphere around the star forms a magnetic X-point geometry when the magnetospheric toroidal current density is sufficiently large or the stellar total current is sufficiently small. A magnetic X-point geometry can be caused by a physical event between the core and crust such as a glitch or a changing magnetic field. An X-point geometry causes a magnetic reconnection which would be an origin of a giant flare of a magnetar. The location of an X-point geometry depends on the size of the twisted region and the shearing model. Equatorial shearing causes an X-point geometry near the stellar surface ($\hat{r}_X \sim 1.59$), but the ring shearing cannot make the X-point geometry near the surface. The X-point geometry in the ring model appears at a distant region near $\hat{r}_X \sim 6.33$. The critical ratio of the poloidal component to toroidal component is estimated to be approximately $|B_t/B_p| \sim 100$. These numerical results show that both Hall MHD secular evolution and magnetospheric dynamical evolution would be affected by the magnetic field configurations of other regions and the core-crust boundary conditions. We need to consider core, crustal, and magnetospheric magnetic field configurations simultaneously in order to investigate magnetar physics.

ACKNOWLEDGEMENTS

The authors would like to thank an anonymous reviewer for useful comments and suggestions that helped us to improve this paper. KF would like to thank the members of plasma seminar at the NAOJ for the very exciting discussion and drinks after the seminar. KF would like to thank Prof. T. Terasawa and Prof. S. Yamada for their valuable and useful comments. KF was supported by Grant-in-aid for JSPS Fellows. KF and SK are supported by Grant-in-Aid for Scientific Research on Innovative Areas, No. 24103006.

REFERENCES

- Antoniadis J., Freire P. C. C., Wex N., Tauris T. M., Lynch R. S., van Kerkwijk M. H., Kramer M., Bassa C., Dhillon V. S., Driebe T., Hessels J. W. T., Kaspi V. M., Kondratiev V. I., Langer N., Marsh T. R., McLaughlin M. A., Pennucci T. T., Ransom S. M., Stairs I. H., van Leeuwen J., Verbiest J. P. W., Whelan D. G., 2013, *Science*, 340, 448
- Baym G., Pethick C., Pikes D., 1969, *Nature*, 224, 674
- Beloborodov A. M., Thompson C., 2007, *ApJ*, 657, 967

- Bocquet M., Bonazzola S., Gourgoulhon E., Novak J., 1995, *A&A*, 301, 757
- Bonazzola S., Gourgoulhon E., 1996, *A&A*, 312, 675
- Braithwaite J., 2009, *MNRAS*, 397, 763
- Braithwaite J., Spruit H. C., 2006, *A&A*, 450, 1097
- Chandrasekhar S., 1956, *Proceedings of the National Academy of Science*, 42, 1
- Chandrasekhar S., Fermi E., 1953, *ApJ*, 118, 116
- Chandrasekhar S., Prendergast K. H., 1956, *Proceedings of the National Academy of Science*, 42, 5
- Ciolfi R., Ferrari V., Gualtieri L., 2010, *MNRAS*, 406, 2540
- Ciolfi R., Ferrari V., Gualtieri L., Pons J. A., 2009, *MNRAS*, 397, 913
- Ciolfi R., Rezzolla L., 2013, *MNRAS*, 435, L43
- Cumming A., Arras P., Zweibel E., 2004, *ApJ*, 609, 999
- Demorest P. B., Pennucci T., Ransom S. M., Roberts M. S. E., Hessels J. W. T., 2010, *Nature*, 467, 1081
- Douchin F., Haensel P., 2001, *A&A*, 380, 151
- Duez V., Braithwaite J., Mathis S., 2010, *ApJ*, 724, L34
- Duez V., Mathis S., 2010, *A&A*, 517, A58+
- Duncan R. C., Thompson C., 1992, *ApJ*, 392, L9
- Ferraro V. C. A., 1954, *ApJ*, 119, 407
- Fujisawa K., Eriguchi Y., 2013, *MNRAS*, 432, 1245
- Fujisawa K., Takahashi R., Yoshida S., Eriguchi Y., 2013, *MNRAS*, 431, 1453
- Fujisawa K., Yoshida S., Eriguchi Y., 2012, *MNRAS*, 422, 434
- Geppert U., Rheinhardt M., 2002, *A&A*, 392, 1015
- Glampedakis K., Andersson N., Lander S. K., 2012, *MNRAS*, 420, 1263
- Glampedakis K., Lander S. K., Andersson N., 2014, *MNRAS*, 437, 2
- Goldreich P., Reisenegger A., 1992, *ApJ*, 395, 250
- Gourgouliatos K. N., Cumming A., 2014, *MNRAS*, 438, 1618
- Gourgouliatos K. N., Cumming A., Reisenegger A., Armaza C., Lyutikov M., Valdivia J. A., 2013, *MNRAS*, 434, 2480
- Gourgouliatos K. N., Lynden-Bell D., 2008, *MNRAS*, 391, 268
- Haensel P., Potekhin A. Y., Yakovlev D. G., eds., 2007, *Astrophysics and Space Science Library*, Vol. 326, *Neutron Stars I: Equation of State and Structure*
- Haskell B., Samuelsson L., Glampedakis K., Andersson N., 2008, *MNRAS*, 385, 531
- Hollerbach R., Rüdiger G., 2002, *MNRAS*, 337, 216
- , 2004, *MNRAS*, 347, 1273
- Ioka K., Sasaki M., 2004, *ApJ*, 600, 296
- Jones P. B., 1988, *MNRAS*, 233, 875
- Kiuchi K., Kotake K., 2008, *MNRAS*, 385, 1327
- Kiuchi K., Yoshida S., 2008, *Phys. Rev. D*, 78, 044045
- Kojima Y., Kisaka S., 2012, *MNRAS*, 421, 2722
- Konno K., Obata T., Kojima Y., 1999, *A&A*, 352, 211
- Lander S. K., 2013, *Physical Review Letters*, 110, 071101
- , 2014, *MNRAS*, 437, 424
- Lander S. K., Andersson N., Glampedakis K., 2012, *MNRAS*, 419, 732
- Lander S. K., Jones D. I., 2009, *MNRAS*, 395, 2162
- Masada Y., Nagataki S., Shibata K., Terasawa T., 2010, *PASJ*, 62, 1093
- Matsumoto J., Masada Y., Asano E., Shibata K., 2011, *ApJ*, 733, 18
- Miketinac M. J., 1973, *Ap&SS*, 22, 413
- , 1975, *Ap&SS*, 35, 349
- Naito T., Kojima Y., 1994, *MNRAS*, 266, 597
- Ostriker J. P., Hartwick F. D. A., 1968, *ApJ*, 153, 797
- Parfrey K., Beloborodov A. M., Hui L., 2013, *ApJ*, 774, 92
- Perna R., Pons J. A., 2011, *ApJ*, 727, L51
- Pons J. A., Geppert U., 2007, *A&A*, 470, 303
- Pons J. A., Link B., Miralles J. A., Geppert U., 2007, *Physical Review Letters*, 98, 071101
- Prendergast K. H., 1956, *ApJ*, 123, 498
- Reisenegger A., Benguria R., Prieto J. P., Araya P. A., Lai D., 2007, *A&A*, 472, 233
- Rheinhardt M., Geppert U., 2002, *Physical Review Letters*, 88, 101103
- Rheinhardt M., Konenkov D., Geppert U., 2004, *A&A*, 420, 631
- Shalybkov D. A., Urpin V. A., 1997, *A&A*, 321, 685
- Spruit H. C., 2009, in *Proceedings IAU Symposium*, Vol. 259, *Cosmic Magnetic Fields: From Planets, to Stars and Galaxies*, K. G. Strassmeier, A. G. Kosovichev & J. E. Beckman, ed., pp. 61–73
- Takahashi H. R., Asano E., Matsumoto R., 2009, *MNRAS*, 394, 547
- , 2011, *MNRAS*, 414, 2069
- Thompson C., Duncan R. C., 1995, *MNRAS*, 275, 255
- , 2001, *ApJ*, 561, 980
- Thompson C., Lyutikov M., Kulkarni S. R., 2002, *ApJ*, 574, 332
- Tomimura Y., Eriguchi Y., 2005, *MNRAS*, 359, 1117
- Urpin V. A., Shalybkov D. A., 1995, *A&A*, 294, 117
- Viganò D., Pons J. A., 2012, *MNRAS*, 425, 2487
- Viganò D., Pons J. A., Miralles J. A., 2011, *A&A*, 533, A125
- , 2012, *Computer Physics Communications*, 183, 2042
- Viganò D., Rea N., Pons J. A., Perna R., Aguilera D. N., Miralles J. A., 2013, *MNRAS*, 434, 123
- Wentzel D. G., 1961, *ApJ*, 133, 170
- Woltjer L., 1959a, *ApJ*, 130, 400
- , 1959b, *ApJ*, 130, 405
- Yoshida S., Eriguchi Y., 2006, *ApJ*, 164, 156
- Yoshida S., Kiuchi K., Shibata M., 2012, *Phys. Rev. D*, 86, 044012
- Yoshida S., Yoshida S., Eriguchi Y., 2006, *ApJ*, 651, 462

APPENDIX A: DERIVATIONS OF THE BASIC EQUATIONS

The evolution of the magnetic field is governed by the induction equation

$$\frac{\partial}{\partial t} \mathbf{B} = -c \nabla \times \mathbf{E}. \quad (\text{A1})$$

The electrical field in the crust is expressed as (Goldreich & Reisenegger 1992),

$$\mathbf{E} = \frac{\mathbf{j}}{\sigma} + \frac{1}{en_e c} (\mathbf{B} \times \mathbf{j}) + \nabla\mu, \quad (\text{A2})$$

where σ is the electric conductivity, n_e is the electron number density, e is the charge of an electron and c is the speed of light. $\nabla\mu$ denotes the gradient of the total chemical potential term. Therefore, the Hall MHD evolutionary equation is

$$\frac{\partial}{\partial t} \mathbf{B} = -\nabla \times \left(\frac{c^2}{4\pi\sigma} \nabla \times \mathbf{B} \right) + \nabla \times \left[\frac{c}{4\pi en_e} \mathbf{B} \times (\nabla \times \mathbf{B}) \right]. \quad (\text{A3})$$

The first term on the right hand side is the Ohmic diffusion and the second is the Hall drift. If the Hall drift is much faster than the Ohmic diffusion and the magnetic field reaches nearly stationary, the left hand side and the first term on the right hand side of the equation vanishes. The evolutionary equation becomes the Hall equilibrium condition as follows:

$$\nabla \times \left[\frac{c}{4\pi en_e} \mathbf{B} \times (\nabla \times \mathbf{B}) \right] = 0. \quad (\text{A4})$$

Since c and e are physical constants, this implies the presence of a scalar function S as

$$\nabla S = \frac{1}{n_e} \left(\mathbf{B} \times \frac{\mathbf{j}}{c} \right). \quad (\text{A5})$$

From the axisymmetry condition, we obtain

$$\frac{1}{n_e} \left(\mathbf{B} \times \frac{\mathbf{j}}{c} \right)_\varphi = 0. \quad (\text{A6})$$

These conditions are the same as the stationary conditions in the barotropic axisymmetric MHD except for n_e . The physical dimensions of these equations are different, but the physical meaning is almost identical. The Hall drift term originates from the Lorentz force of the electron. Therefore, we obtain the following condition from the toroidal component of Eq. (A6)

$$\nabla\Psi \times \nabla I = 0 \Leftrightarrow I \equiv I(\Psi). \quad (\text{A7})$$

From the meridional component of Eq. (A5), the functional form of the toroidal current density is obtained as

$$4\pi \frac{j_\varphi}{c} = \frac{I(\Psi)I'(\Psi)}{r \sin\theta} + 4\pi n_e r \sin\theta S(\Psi), \quad (\text{A8})$$

$$\text{where } I' = \frac{dI}{d\Psi}.$$

APPENDIX B: GENERATING FUNCTION FOR THE LEGENDRE POLYNOMIAL

The solution of the Poisson equation,

$$\Delta(A(r, \theta) \sin\varphi) = -4\pi j(r, \theta) \sin\varphi, \quad (\text{B1})$$

is expressed by the $m = 1$ Legendre function $P_n^1(\cos\theta)$ in an axisymmetric system as follows:

$$\begin{aligned} A(r, \theta) \sin\varphi &= \sum_{n=1}^{\infty} \frac{2P_n^1(\cos\theta)}{n(n+1)} \int_0^\infty r'^2 f_n(r, r') dr' \int_0^\pi \sin\theta P_n^1(\cos\theta') d\theta' \int_0^{2\pi} \cos(\varphi - \varphi') d\varphi' j(r', \theta') \sin\varphi' \\ &+ \sum_{n=1}^{\infty} \left(a_n r^{n+1} P_n^1(\cos\theta) + b_n r^{-n} P_n^1(\cos\theta) \right) \sin\varphi, \\ \Rightarrow A(r, \theta) &= 2\pi \sum_{n=1}^{\infty} \frac{P_n^1(\cos\theta)}{n(n+1)} \int_0^\infty r'^2 f_n(r, r') dr' \int_0^\pi \sin\theta P_n^1(\cos\theta') d\theta' j(r', \theta'), \\ &+ \sum_{n=1}^{\infty} \left(a_n r^{n+1} P_n^1(\cos\theta) + b_n r^{-n} P_n^1(\cos\theta) \right), \end{aligned} \quad (\text{B2})$$

where P_n^1 is the n th associated Legendre function and $f_n(r, r')$ is the following function:

$$f_n(r, r') = \begin{cases} \frac{1}{r} \left(\frac{r'}{r} \right)^n & (r \geq r') \\ \frac{1}{r'} \left(\frac{r}{r'} \right)^n & (r' > r) \end{cases}, \quad (\text{B3})$$

and the last terms of the right hand side are homogeneous general solutions to Eq.(B1).

APPENDIX C: DIMENSIONLESS FORMS

Using four quantities (r_s , ρ_{\max} , n_c and S_{\max}), we obtain dimensionless forms of physical quantities as follows:

$$\hat{F} = \frac{F}{n_c |S_{\max}| / \rho_{\max}}, \quad (\text{C1})$$

$$\hat{B} = \frac{B}{r_s^2 n_c |S_{\max}|}, \quad (\text{C2})$$

$$\hat{\Psi} = \frac{\Psi}{r_s^4 n_c |S_{\max}|}, \quad (\text{C3})$$

$$\hat{I} = \frac{I}{r_s^5 n_c |S_{\max}|}, \quad (\text{C4})$$

$$\hat{j} = \frac{j_\varphi / c}{r_s n_c |S_{\max}|}. \quad (\text{C5})$$

The functional forms of F and S also become dimensionless as shown below:

$$\hat{S}(\hat{\Psi}) = \hat{S}_0, \quad (\text{C6})$$

$$\hat{F}(\hat{\Psi}) = \hat{F}_0. \quad (\text{C7})$$

In particular, noted that the value of \hat{S}_0 is 1 or -1 from its definition.

APPENDIX D: ANALYTICAL SOLUTIONS

We show here the analytical solution of each model. When the magnetic field is purely poloidal ($\hat{I} = 0$) and the functional forms are $\hat{S} = \hat{S}_0$ and $\hat{F} = \hat{F}_0$, we can easily calculate analytical solutions. We can obtain the exact solutions by integrating \hat{j}_φ throughout the entire region. We set $\hat{\rho} = \hat{\rho}_0$ and $\hat{n}_e = \hat{n}_0$, but we can also obtain the solutions with arbitrary ρ and n_e distributions. The functional form of the toroidal current density becomes

$$\hat{j}_\varphi = \begin{cases} \hat{\rho}_0 \hat{F}_0 \hat{r} \sin \theta & (0 \leq \hat{r} < \hat{r}_{in}) \\ \hat{n}_0 \hat{S}_0 \hat{r} \sin \theta & (\hat{r}_{in} \leq \hat{r} \leq \hat{r}_s) \\ 0 & (\hat{r}_s < \hat{r}) \end{cases}. \quad (\text{D1})$$

Now, we can obtain the analytical solutions by calculating the integral of Eq. (12).

D1 Model I

The magnetic field within the core ($0 \leq \hat{r} < \hat{r}_{in}$) is excluded by the Meissner effect in this model. The current density also does not exist in the core. Therefore, we fixed $\hat{F}_0 = 0$. Then the integration of the Green function is expressed (see App. B) by

$$\begin{aligned} \hat{\Psi}(\hat{r}, \theta) &= 2\pi \hat{r} \sin \theta \hat{S}_0 \sum_{n=1}^{\infty} \frac{P_n^1(\cos \theta)}{n(n+1)} \int_0^\infty f_n(\hat{r}, \hat{r}') \hat{r}'^2 d\hat{r}' \int_0^\pi P_n^1(\cos \theta') \sin \theta' d\theta' (\hat{n}_0 \hat{r}' \sin \theta') \\ &+ \sum_{n=1}^{\infty} (a_n \hat{r}^{n+1} P_n^1(\cos \theta) + b_n \hat{r}^{-n} P_n^1(\cos \theta)) \sin \theta. \end{aligned} \quad (\text{D2})$$

Since the number density profile is independent of θ , we can integrate the θ component. From the orthogonality of the associated Legendre function,

$$\int_0^\pi \sin \theta' P_n^1(\cos \theta') P_n^1(\cos \theta') d\theta' = 2 \frac{n(n+1)}{2n+1}, \quad (\text{D3})$$

the higher terms ($n \geq 2$) must vanish. Then, the equation becomes

$$\hat{\Psi}(\hat{r}, \theta) = \frac{4\pi}{3} \hat{r} \sin^2 \theta \hat{S}_0 \hat{n}_0 \int_0^\infty f_1(\hat{r}, \hat{r}') \hat{r}'^3 d\hat{r}' + (a_1 \hat{r}^2 + b_1 \hat{r}^{-1}) \sin^2 \theta. \quad (\text{D4})$$

The electrons exit within a finite region ($\hat{r}_{in} \leq \hat{r} \leq \hat{r}_s$) of the star. Then, the \hat{r} integral is classified into three types, – the inner vacuum solution, the internal solution and the outer vacuum solution:

$$\int_0^\infty f_1(\hat{r}, \hat{r}') \hat{r}'^2 d\hat{r}' = \begin{cases} \hat{r} \left(\int_{\hat{r}_{in}}^{\hat{r}_s} \hat{r}'^2 d\hat{r}' \right) = \frac{1}{2} \hat{r}_s^2 \hat{r}^2 - \frac{1}{2} \hat{r}_{in}^2 \hat{r}^2 & (0 \leq \hat{r} \leq \hat{r}_{in}) \\ \hat{r} \left(\int_{\hat{r}_{in}}^{\hat{r}} \frac{\hat{r}'^4}{\hat{r}^2} d\hat{r}' + \int_{\hat{r}}^{\infty} \hat{r}'^2 d\hat{r}' \right) = \left(\frac{1}{5} \hat{r}^4 - \frac{1}{5} \frac{\hat{r}_{in}^5}{\hat{r}} \right) + \left(\frac{1}{2} \hat{r}_s^2 \hat{r}^2 - \frac{1}{2} \hat{r}^4 \right) & (\hat{r}_{in} \leq \hat{r} \leq \hat{r}_s) \\ \hat{r} \left(\int_{\hat{r}_{in}}^{\hat{r}_s} \frac{\hat{r}'^4}{\hat{r}^2} d\hat{r}' \right) = \left(\frac{1}{5} \frac{\hat{r}_s^5}{\hat{r}} - \frac{1}{5} \frac{\hat{r}_{in}^5}{\hat{r}} \right) & (\hat{r}_s \leq \hat{r}) \end{cases} \quad (D5)$$

If we neglect the homogeneous terms, there is no current sheet in the system and the crustal magnetic fields penetrate the core. Due to the Meissner effect in this model, the magnetic field cannot penetrate within the $\hat{r} \leq \hat{r}_{in}$ region, and so we must impose the boundary condition $\hat{\Psi}(\hat{r}_{in}, \theta) = 0$. We need to choose the coefficients of the homogeneous terms in this case. The terms represent the contribution from the toroidal current sheet on $\hat{r} = \hat{r}_{in}$ (Fujisawa & Eriguchi 2013). Therefore, we incorporate the toroidal current sheet in $r = r_{in}$ in order to satisfy the boundary condition $\hat{\Psi}(\hat{r}_{in}, \theta) = 0$ as follows:

$$\hat{\Psi}(\hat{r}, \theta) = \begin{cases} \frac{4\pi \hat{S}_0 \hat{n}_0}{3} \sin^2 \theta \left[\frac{1}{2} \hat{r}_s^2 \hat{r}^2 - \frac{1}{2} \hat{r}_{in}^2 \hat{r}^2 \right] + \hat{j}_0 \hat{r}^2 \sin^2 \theta = 0 & (0 \leq \hat{r} \leq \hat{r}_{in}) \\ \frac{4\pi \hat{S}_0 \hat{n}_0}{3} \sin^2 \theta \left[\left(\frac{1}{5} \hat{r}^4 - \frac{1}{5} \frac{\hat{r}_{in}^5}{\hat{r}} \right) + \left(\frac{1}{2} \hat{r}_s^2 \hat{r}^2 - \frac{1}{2} \hat{r}^4 \right) \right] + \hat{j}_0 \hat{r}_{in}^3 \hat{r}^{-1} \sin^2 \theta & (\hat{r}_{in} \leq \hat{r} \leq \hat{r}_s) \\ \frac{4\pi \hat{S}_0 \hat{n}_0}{3} \sin^2 \theta \left[\left(\frac{1}{5} \frac{\hat{r}_s^5}{\hat{r}} - \frac{1}{5} \frac{\hat{r}_{in}^5}{\hat{r}} \right) \right] + \hat{j}_0 \hat{r}_{in}^3 \hat{r}^{-1} \sin^2 \theta & (\hat{r}_s \leq \hat{r}) \end{cases} \quad (D6)$$

where \hat{j}_0 is the strength of the toroidal current sheet ($\hat{j}_0 = a_1 = \hat{r}_{in}^3 b_1$). Since the a_1 term is the inner solution and the b_1 term is the outer solution, a_1 is determined by the boundary condition $\hat{\Psi}(\hat{r}_{in}, \theta) = 0$ and the explicit form of \hat{j}_0 is

$$\hat{j}_0 = \frac{2\pi \hat{S}_0 \hat{n}_0}{3} (\hat{r}_{in}^2 - \hat{r}_s^2). \quad (0 < \hat{r}_{in}) \quad (D7)$$

Also, the sign of \hat{j}_0 is negative. This means that to exclude the magnetic field from the crustal toroidal current, the Meissner effect equals the effective *negative current sheet* on the core-crust boundary (see Fig. 5 in Bonazzola & Gourgoulhon 1996).

D2 Model II

Model II is the crustal current model, but it does not have a current sheet on the core-crust boundary. Therefore, the solution is shown below:

$$\hat{\Psi}(\hat{r}, \theta) = \begin{cases} \frac{4\pi \hat{S}_0 \hat{n}_0}{3} \sin^2 \theta \left[\frac{1}{2} \hat{r}_s^2 \hat{r}^2 - \frac{1}{2} \hat{r}_{in}^2 \hat{r}^2 \right] & (0 \leq \hat{r} \leq \hat{r}_{in}) \\ \frac{4\pi \hat{S}_0 \hat{n}_0}{3} \sin^2 \theta \left[\left(\frac{1}{5} \hat{r}^4 - \frac{1}{5} \frac{\hat{r}_{in}^5}{\hat{r}} \right) + \left(\frac{1}{2} \hat{r}_s^2 \hat{r}^2 - \frac{1}{2} \hat{r}^4 \right) \right] & (\hat{r}_{in} \leq \hat{r} \leq \hat{r}_s) \\ \frac{4\pi \hat{S}_0 \hat{n}_0}{3} \sin^2 \theta \left[\left(\frac{1}{5} \frac{\hat{r}_s^5}{\hat{r}} - \frac{1}{5} \frac{\hat{r}_{in}^5}{\hat{r}} \right) \right] & (\hat{r}_s \leq \hat{r}) \end{cases} \quad (D8)$$

D3 Models III & IV

These models have both a core current and a crustal current. Therefore, the solutions are described by the sum of the core current magnetic field $\hat{\Psi}_{co}$ and the crustal current magnetic field $\hat{\Psi}_{cr}$. The crustal current magnetic field $\hat{\Psi}_{cr}$ is equal to the model II solution. We can easily obtain the profile of $\hat{\Psi}_{co}$. The solution is

$$\hat{\Psi}_{co}(\hat{r}, \theta) = \begin{cases} \frac{4\pi \hat{F}_0 \hat{\rho}_0}{3} \sin^2 \theta \left[\left(\frac{1}{5} \hat{r}^4 \right) + \left(\frac{1}{2} \hat{r}_{in}^2 \hat{r}^2 - \frac{1}{2} \hat{r}^4 \right) \right] & (0 \leq \hat{r} < \hat{r}_{in}) \\ \frac{4\pi \hat{F}_0 \hat{\rho}_0}{3} \sin^2 \theta \left[\left(\frac{1}{5} \frac{\hat{r}_{in}^5}{\hat{r}} \right) \right] & (\hat{r}_{in} \leq \hat{r}) \end{cases} \quad (D9)$$

As a result, the general solutions of models III and IV are

$$\hat{\Psi}(\hat{r}, \theta) = \begin{cases} \frac{4\pi}{3} \sin^2 \theta \left[\hat{F}_0 \hat{\rho}_0 \left\{ \left(\frac{1}{5} \hat{r}^4 \right) + \left(\frac{1}{2} \hat{r}_{in}^2 \hat{r}^2 - \frac{1}{2} \hat{r}^4 \right) \right\} + \hat{S}_0 \hat{n}_0 \left\{ \frac{1}{2} \hat{r}_s^2 \hat{r}^2 - \frac{1}{2} \hat{r}_{in}^2 \hat{r}^2 \right\} \right] + \hat{j}_0 \hat{r}^2 \sin^2 \theta & (0 \leq \hat{r} < \hat{r}_{in}), \\ \frac{4\pi}{3} \sin^2 \theta \left[\hat{F}_0 \hat{\rho}_0 \left(\frac{1}{5} \frac{\hat{r}_{in}^5}{\hat{r}} \right) + \hat{S}_0 \hat{n}_0 \left\{ \left(\frac{1}{5} \hat{r}^4 - \frac{1}{5} \frac{\hat{r}_{in}^5}{\hat{r}} \right) + \left(\frac{1}{2} \hat{r}_s^2 \hat{r}^2 - \frac{1}{2} \hat{r}^4 \right) \right\} \right] + \hat{j}_0 \hat{r}_{in}^3 \hat{r}^{-1} \sin^2 \theta & (\hat{r}_{in} \leq \hat{r} \leq \hat{r}_s) \\ \frac{4\pi}{3} \sin^2 \theta \left[\hat{F}_0 \hat{\rho}_0 \left(\frac{1}{5} \frac{\hat{r}_{in}^5}{\hat{r}} \right) + \hat{S}_0 \hat{n}_0 \left\{ \frac{1}{5} \frac{\hat{r}_s^5}{\hat{r}} - \frac{1}{5} \frac{\hat{r}_{in}^5}{\hat{r}} \right\} \right] + \hat{j}_0 \hat{r}_{in}^3 \hat{r}^{-1} \sin^2 \theta & (\hat{r}_s \leq \hat{r}) \end{cases} \quad (D10)$$

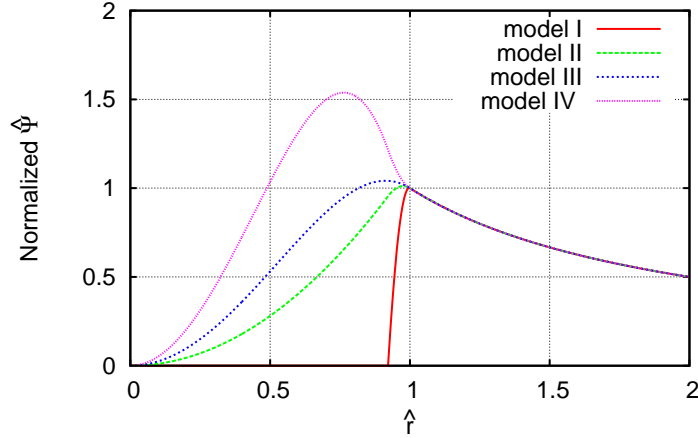


Figure D1. The $\hat{\Psi}$ profiles of each model on the equatorial plane. They are normalized by the value of $\hat{\Psi}(\hat{r}_s, \pi/2)$. The core-crust boundary is $\hat{r} = 0.921875$.

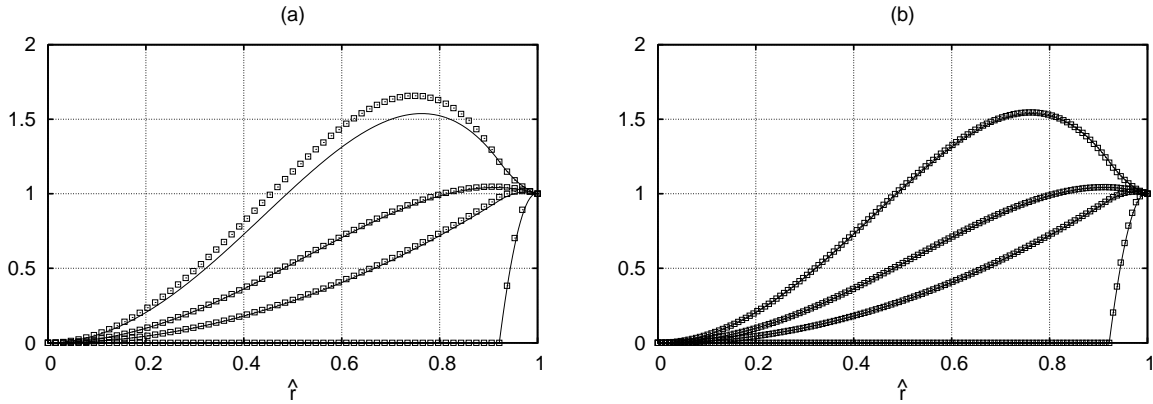


Figure E1. Numerical (points) and analytical (lines) solutions of each model. Left panel(a): $N_{r1} = 65$ ($\hat{r} = [0 : 1]$), $N_{\theta} = 257$ ($\theta = [0 : \pi]$) solutions. Right panel(b): $N_{r1} = 129$, $N_{\theta} = 257$ solutions. The solutions in (b) represent the analytical solutions very well.

where $\hat{F}_0 \hat{S}_0 > 0$ (model III) and $\hat{F}_0 \hat{S}_0 < 0$ (model IV). Note that models III and IV can have an arbitrary current sheet on the core-crust boundary. The last term represents the contribution from the dipole current sheet (see Fujisawa & Eriguchi 2013). \hat{j}_0 denotes the strength of the current sheet.

D4 The magnetic field configurations of each model

We show here some graphs of the analytical solutions. We set $\hat{r}_s = 1$ and $\hat{r}_{in} = 0.921875$. The functional parameters are $\hat{S}_0 = 1$, $\hat{F}_0 = 1$ (model III) and $\hat{S}_0 = -1$, $\hat{F}_0 = 1$ (model IV). We show the contours of $\hat{\Psi}$ in Fig. 1. Fig. D1 displays profiles of Ψ on the equatorial plane normalized by its surface value.

APPENDIX E: ACCURACY VERIFICATION

We checked the accuracy of the numerical solutions. We can see the differences between the analytical solutions (App. D) and numerical solutions by changing the mesh numbers (a: $N_{r1} = 65$, b: $N_{r1} = 129$ in Fig. E1), where N_{r1} refers to the mesh numbers within the stellar region ($\hat{r} = [0 : 1]$). We display the four numerical and analytical solutions (models I, II, III and IV) in Fig. E1. As seen in Fig. E1, the numerical solutions in panel (b) represent the analytical solutions very well. In actual numerical calculations which are tabulated and displayed in this paper, we use $N_{\theta} = 1025$ ($\theta = [0 : \pi]$), $N_{r1} = 513$, $N_{r2} = 513$ ($\hat{r} = [1 : 2]$ Sec. 3.1) and $N_{r2} = 513$, ($\hat{r} = [1 : 16]$ Sec. 3.2, 3.3) in order to obtain more accurate numerical results. As for the Legendre polynomial, we sum of $P_n^1(\cos \theta)$ to $n_{\max} = 21$ in all numerical calculations.

APPENDIX F: DISSIPATION TIMESCALE OF THE CURRENT SHEET AT THE CORE-CRUST INTERFACE

The dissipation timescale of the current sheet at the core-crust interface is important. If the dissipation timescale is much shorter than the Hall timescale, our numerical result with a current sheet is not a possible configuration. If the value of the magnetic Reynolds number is $\mathcal{R}_m = 1000$ (Eq. 1), the Hall timescale is 1000 times shorter than the Ohmic dissipation timescale. Since the Ohmic dissipation timescale is given by

$$t_{\text{Ohm}} = \frac{4\pi\sigma\delta r_c^2}{c^2} \sim 5 \times 10^7 \left(\frac{\sigma}{10^{25}\text{s}^{-1}} \right) \left(\frac{\Delta r_c}{0.1r_s} \right)^2 \text{ yr.}, \quad (\text{F1})$$

the Hall timescale is estimated as

$$t_{\text{Hall}} = \mathcal{R}_m t_{\text{Ohm}} \sim 5 \times 10^4 \text{ yr.}, \quad (\text{F2})$$

where Δr_c is a width of the crust and $r_s \sim 10^6$ cm is the stellar radius.

The dissipation timescale of the current sheet depends on both the width of the current sheet and the electrical conductivity at the interface, but the exact value of the electrical conductivity is still not clear. We assumed that the value equal to that of the core electrical conductivity $\sigma \sim 10^{29}\text{s}^{-1}$ (Baym et al. 1969; Haensel et al. 2007). If the width of the current sheet is $10^{-4}r_s$, then the dissipation timescale of the current sheet $t_{\text{dis.}}$ is evaluated by

$$t_{\text{dis.}} = \frac{4\pi\sigma\Delta r_{cs}^2}{c^2} \sim 5 \times 10^5 \left(\frac{\sigma}{10^{29}\text{s}^{-1}} \right) \left(\frac{\Delta r_{cs}}{10^{-4}r_s} \right)^2 \text{ yr.}, \quad (\text{F3})$$

where Δr_{cs} is the width of the current sheet. The grid number of the star is $N_r = 513$ (see App. E) and the grid size is $\Delta r = r_s/512 \sim 2 \times 10^{-3}r_s$ in this paper. Although Δr_{cs} is much smaller than the grid size Δr , the dissipation timescale $t_{\text{dis.}}$ is much larger than the Hall timescale t_{Hall} . Therefore, we can treat the current sheet as a δ function (Eq. 14) and consider the magnetar models with a current sheet at the core-crust interface in this paper as possible configurations.